The nonlinearity of scattering waves due to interaction between focusing waves and floating production storage and offloading ⊘

Yuan Zhuang (庄园) ⓘ ; Weiwen Zhao (赵伟文) ⓘ ; Decheng Wan (万德成) ✉ ⓘ

Check for updates

CrossMark

View Online

Export Citation

The nonlinearity of scattering waves due to interaction between focusing waves and floating production storage and offloading

Yuan Zhuang (庄园), [iD] Weiwen Zhao (赵伟文), [iD] and Decheng Wan (万德成)[a] [iD]

AFFILIATIONS

Computational Marine Hydrodynamics Lab (CMHL), School of Naval Architecture, Ocean and Civil Engineering,
Shanghai Jiao Tong University, Shanghai, China

Note: This paper is part of the special topic, Recent Advances in Marine Hydrodynamics.
[a]Author to whom correspondence should be addressed: dcwan@sjtu.edu.cn. URL: http://dcwan.sjtu.edu.cn/

ABSTRACT

The study of the full-scale wave–structure interaction is essential to our understanding of the nonlinear characteristics of offshore structures in real-sea states. This paper deals with full-scale numerical studies of the interactions between focusing waves and a fixed floating production storage and offloading (FPSO) in an efficient potential-viscous coupled method. The potential-viscous method combines in-house computational fluid dynamics code developed at Shanghai Jiao Tong University (SJTU) for naval architecture and ocean engineering (naoe) based on an open field operation and manipulation (FOAM), i.e., naoe-FOAM-SJTU solver, with high-order spectral method. The approach is verified on a model-scaled case and shows reasonably good agreement with experimental data. A phase-separation method and a dynamic mode decomposition method are utilized to extract linear and higher-order harmonic components from the scattering waves. The scattering waves around the FPSO are found to affect the higher-order harmonic components. Two kinds of scale ratios are considered to magnify the focusing wave and FPSO by 10 and 100 times to discuss the scale effect, both non-breaking and green water conditions are included to investigate the flow phenomenon. The harmonic components of scattering waves are not proportional to the scale ratio, and the scale effects influence more on higher-order harmonic components. The third- and fourth-order harmonic components of scattering waves around the FPSO in large-scale cases are obvious.

Published under an exclusive license by AIP Publishing. https://doi.org/10.1063/5.0165661

I. INTRODUCTION

For many large offshore structures, such as floating production storage and offloading (FPSO) platforms, wind turbine foundations and other offshore platforms are easily vulnerable to hostile environment. The severe sea state causes damage to structures, thus may lead to work stoppages. Therefore, research on the interaction between structures and rogue waves is becoming increasingly popular. Focusing wave consists of a large number of wave components of different frequencies with considerable randomness, so the application of focusing waves can lead to rogue waves.

It has been suggested that an input wave composed of linear components can cause nonlinear wave–structure interactions. For example, Swan and Sheikh[1] discovered the nonlinear scattering waves under the interaction between a cylinder and the steep regular waves. Some researchers considered the nonlinearity as wave–wave interaction or nonlinear wave–structure interaction during the wave evolution. Therefore,

the evolved higher-harmonic peak frequency of incident waves can cause nonlinear response such as springing (second-order domination) or ringing (higher-order domination).[2] Since it is a classical structure and a simplified random sea state, the interaction between FPSO and focusing waves has been widely studied. Based on the separation of linear and higher-harmonic components of the incident and scattering waves, Mai et al.[3] investigated the nonlinearity of the scattering waves around different lengths of the FPSO under different headings or steepness of the focusing waves. They found that the second and third-harmonics were strongest in medium length model, while the third- and fourth-harmonic diffracted waves could be relevant to ringing-type responses. Chen et al.[4] discussed the harmonic nonlinear force on different types of FPSO-shaped bodies under various wave conditions. They concluded that the harmonic forces depended on the wave steepness and the bow diameter. Huo et al.[5] studied the nonlinear motion and slamming forces on cylindrical FPSO under wave–current interaction.

There have been many measurements to deal with FPSO interacting with focusing waves. Experiments have been conducted in laboratory wave tanks applying wave paddles to generate focusing waves. According to Chaplin,[6] experimental approaches in generating focusing waves can be identified as phase speed method, the reverse dispersion method and the group celerity method. The experimental method has the advantage of providing accurate and reliable elevation. However, due to scale effects and incomplete flow information, the physical test reaches its limitations. With the development of computer science, numerical modeling became the essential approach in studying the interaction of focusing wave and structures. In the early days, potential theory was popular in solving wave–structure interactions. Through simplifying Navier–Stokes equations, potential theory solves the problem without viscous and rotational feature. Therefore, the calculations in potential theory are always very fast. The original potential theory is disable in solving strongly nonlinear effects or steep waves. Therefore, changes are developed in fully nonlinear potential theory. Engsig-Karup and Eskilsson[7] applied a stabilized spectral element method (SEM) to simulate a FPSO in focusing waves.

Computational fluid dynamics (CFD) have been widely used in recent years because of its ability to simulate strongly nonlinear wave phenomena such as wave breaking or green water, as well as to solve nonlinear structure motion. The work on focusing wave–structure interaction in CFD implements Navier–Stokes equations. Xie et al.[8] developed an in-house solver using finite volume method (FVM) and high resolution volume of fluid (VOF) scheme CICSAM (compressive interface capturing scheme for arbitrary meshes) to solve the focusing wave–structure interaction. They applied LES (large-eddy simulation) as the turbulence model. Zhuang and Wan[9] implemented CMHL in-house solver naoe-FOAM-Shanghai Jiao Tong University (SJTU) to simulate focusing waves interaction with FPSO. The wave generation was a velocity inlet boundary condition and wave absorption were done by adding source terms. The CFD method has its advantage in dealing with strongly nonlinear phenomenon, but this method needs huge computational resources. For the simulation of focusing waves, the CFD method requires large computational domain and long-time duration; thus, it needs more computational resources than other cases.

In recent years, some new coupled methods rise to deal with the wave-interaction problem. To reduce large cost in the CFD method and reserve the feature for solving strongly nonlinear cases in CFD, a potential viscous coupled method is developed. Li et al.[10] combined QALE-FEM (Quasi Arbitrary Lagrangian-Eulerian Finite Element Method) with OpenFOAM using a coupling boundary to generate focusing wave and simulated wave–structure interaction. Higuera et al.[11] used Lagrangian wave model with olaFlow to do the one-way coupling in simulating focusing waves. Gatin et al.[12] applied the SWENSE (spectral wave explicit Navier–Stokes equations) method to combine the potential incident wave and the CFD method. They also simulated focusing waves on fixed-FPSO.

Most studies mentioned above concentrated on model-scale, rarely considered large or full-scale situation. Although the scale effects were small in the wave–structure interaction, when it comes to the nonlinear scattering wave, the influence of viscous cannot be ignored. In this paper, we utilize a coupled potential-viscous method to do the full-scale simulation. The highly efficient method on solving nonlinear propagation wave called the high-order spectral method (HOS)[13] is adopted to combine with CMHL in-house solver naoe-FOAM-

SJTU,[14] which has the huge advantages on full-scale simulation. Section II describes the governing equations of viscous solver and boundary conditions of potential theory solver, while the way they coupled is given. In order to make the results of wave generation closer to physical studies, the reproduction procedure is adopted.

We choose a benchmark test[15] to test the coupled method and the simulation at model-scale. The numerical method verification is illustrated in Sec. III. The comparison between the coupled method with CFD method is given, showing the coupled method a more efficient characteristic. The full-scale simulation and discussion of scale effect are presented in Sec. IV. Two scale ratios are considered, as well as the harmonic components method is adopted to figure out the higher-order harmonic of the scattering waves. The focusing wave of large steepness is considered between model- and full-scale cases, and DMD (dynamic mode decomposition) method is applied to determine the modes of the flow field. Finally, the scattering wave fields and vortices around the FPSO are studied to interpret the harmonic components.

II. NUMERICAL METHOD
A. CFD viscous solver

We adopt SJTU in-house solver naoe-FOAM-SJTU as the viscous solver, which is developed based on the open-source software OpenFOAM. The governing equations are Navier–Stokes equations, and calculate in the whole viscous domain,

$$\nabla \cdot \mathbf{U} = 0, \tag{1}$$

$$\frac{\partial \rho \mathbf{U}}{\partial t} + \nabla \cdot (\rho(\mathbf{U} - \mathbf{U}_g)\mathbf{U}) = -\nabla pd - \mathbf{g} \cdot \mathbf{x}\nabla\rho + \nabla \cdot (\mu_{eff}\nabla\mathbf{U})$$
$$+ (\nabla\mathbf{U}) \cdot \nabla\mu_{eff} + f\sigma, \tag{2}$$

where $\mathbf{U}$ is the velocity field, $\mathbf{U}_g$ is the velocity of grid nodes, $pd = p - \rho\mathbf{g} \cdot \mathbf{x}$ is dynamic pressure, $\mathbf{x}$ stands for the vector of the volumetric center position in one grid cell, $\mu_{eff} = \rho(\nu + \nu_t)$ is effective dynamic viscosity, ν represents kinematic viscosity, and ν_t is eddy viscosity. f_σ is the surface tension term in the two-phase flow model. In this paper, we choose laminar flow as turbulence model.

In the potential-viscous coupled method, the volume of fluid (VOF) method is used to capture the free surface. In the viscous domain, the VOF applies bounded compression techniques to control numerical diffusion. The VOF transport equation is described below:

$$\frac{\partial \alpha}{\partial t} + \nabla \cdot [(\mathbf{U} - \mathbf{U}_g)\alpha] = 0, \tag{3}$$

where α is the volume of fraction, indicating the relative proportion of fluid in each cell, and its value is always between zero and one,

$$\begin{cases} \alpha = 0, & air, \\ \alpha = 1, & water, \\ 0 < \alpha < 1, & interface. \end{cases} \tag{4}$$

In addition, the surface tension term in Eq. (2) is defined as

$$f_\sigma = \sigma\kappa\nabla\alpha, \tag{5}$$

where σ is chosen to be $0.07 \, kg/s^2$, which is the surface tension coefficient. κ is the curvature of surface interface defined as

$$\kappa = -\nabla \cdot (\nabla\alpha/|\nabla\alpha|). \tag{6}$$

In OpenFOAM, a scheme called MULES (multi-dimensional universal limiter for explicit solution) is used to keep the boundedness steady and accurate. We use the upwind scheme to compress the free surface but with large inaccuracy. Therefore, the MULES scheme substitutes Eq. (3) and becomes

$$(\alpha - \alpha^0)\frac{V}{\Delta t} + \sum_f \phi_f \alpha_f = 0, \tag{7}$$

$$(\alpha - \alpha^0)\frac{V}{\Delta t} + \sum_f \phi_f \alpha_f + \sum_f \lambda_f^+ \phi_f^+ (\alpha_H - \alpha_U)$$
$$+ \sum_f \lambda_f^- \phi_f^- (\alpha_H - \alpha_U) = 0, \tag{8}$$

where α_U is in upwind scheme and α_H is in high-order scheme, λ_f^+ is the limiter on $\alpha = 0$ and λ_f^- is the limiter on $\alpha = 1$. ϕ_f^+ is flux out of cells and ϕ_f^- is flux into cells.

The solution of decoupling pressure and velocity implements PIMPLE scheme, which is achieved by the pressure-implicit split operator (PISO) algorithm.[16] OpenFOAM applies non-staggered grids to discrete the computational domain, which is more efficient in three-dimensional solutions.

B. High-order spectral method

High order spectral method (short for HOS) is a mature pseudo-spectral method for solving nonlinear wave equations. With the application of fast Fourier transform, this method shows advantages in fast convergence and efficiency. For the HOS method is a pseudo spectral method, the formulation is based on the velocity potential on the free surface. Thus, the velocity potential can be defined as

$$\phi^s(\mathbf{x}, t) = \phi(\mathbf{x}, \eta(\mathbf{x}, t), t). \tag{9}$$

According to Eq. (9), the dynamic and kinematic free surface boundary conditions are described as[13]

$$\eta_t + \nabla_x \phi^s \cdot \nabla_x \eta - (1 + \nabla_x \eta \cdot \nabla_x \eta)\phi_z(\mathbf{x}, \eta, t) = 0, \tag{10}$$

$$\phi_t^s + \eta + \frac{1}{2}\nabla_x \phi^s \cdot \nabla_x \phi^s - \frac{1}{2}(1 + \nabla_x \eta \cdot \nabla_x \eta)\phi_z^2(\mathbf{x}, \eta, t) = -Pa, \tag{11}$$

where η is the free surface elevation; Pa is the atmosphere pressure; and ϕ^s is the surface potential. Giving a measure of small parameter, the velocity potential and wave surface can reach to the order of that parameter's quantities. When expanding ϕ in a perturbation series and evaluating each order of ϕ on free surface in a Taylor series, then

$$\phi^s(\mathbf{x}, t) = \sum_{m=1}^{M} \sum_{k=0}^{M-m} \frac{\eta^k}{k!} \frac{\partial^k}{\partial z^k} \phi^{(m)}(\mathbf{x}, 0, t). \tag{12}$$

With the known initial conditions, the unknown ϕ in Eq. (12) can be solved.

In this paper, we apply an open-source software based on HOS method to construct the initial wave field. The software is HOS-NWT (Numerical Wave Tank),[17] which is available on Github (https://github.com//LHEEA/HOS-NWT/wiki). The HOS method that we mentioned above focuses on unbounded domain, and the formulation of HOS method is based on periodic boundary condition. The

unbounded domain will make validation of numerical simulations more difficult, for it is hard to compare with experiments.

C. Combined method

In this paper, the combination is a one-way coupling method, thus we only consider one-way communication from potential theory to viscous theory. We build an interface to do the communication based on a relaxation zone from waves2Foam.[18] This relaxation zone is explicit and applies an exponential weight factor. The method of wave generation describes below:

$$\phi_{final} = \alpha_R \phi_{computed} + (1 - \alpha_R)\phi_{target}, \tag{13}$$

where ϕ_{final} is the parameter of flow (wave velocity, elevation, pressure, etc.) in the relaxation zone, $\phi_{computed}$ is the computed value in viscous domain, and ϕ_{target} is the target value from the HOS wave field. α_R is relaxation factor and its value is from 0 to 1.

However, the original results from HOS cannot be used directly in CFD domain. For all the flow parameters are restored in nodes in HOS, it should be transferred from frequency domain to time domain. Meanwhile, as all the flow parameters only exists in free surface in HOS, the information above free surface is also needed when doing the simulation in CFD domain. Thanks to a HOS wrapper program called Grid2Grid,[19] the information is transformed from modes through inverse FFT. Grid2Grid reconstructs the fields in a volume grid and applies splines to do the mesh interpolation. Therefore, after we build the interface to receive the signal from HOS, the flow information can be transferred into the CFD zone. Figure 1 shows the schematic of combination method, including the setup of two kinds of computational zones and the interpolation of two kinds of mesh grids.

The calculation process of combined HOS method and naoe-FOAM-SJTU can be depicted in Fig. 2. To start the simulation, we should work on HOS solver. After the results from HOS are got with wave amplitude as well as velocity, the interpolation and transformation process are implemented. The reconstruction of HOS mesh and communication between HOS and CFD happens during the simulation, but in order to make it clearer, we decompose these processes in sequence. The Grid2Grid helps transfer the information on modes to grids, while CFD builds an interface to receive those flow information. Combining those wave generation modules with our in-house solver naoe-FOAM-SJTU, we can use all these functions in one solver. The wave generations of the combined solver were tested in previous work,[20] and verified the accuracy in generating waves in CFD zone.

Figure 3 shows the domain setup of the coupled method. The coordinate of HOS solver and CFD solver is not matched thus we need to do domain translation to ensure all the CFD domain is inside HOS domain. In HOS domain, the original coordinate is on the left corner of the computational domain, while in CFD domain, the original coordinate is on the bow of the structure to get the force and moments more easily. Therefore, the CFD domain should be translated to avoid unmatched information from HOS domain. The communication domain is a virtual domain of CFD, the information from HOS is transferred to this place. This kind of setup gives a lot of convenience in simulating the focusing wave condition. In traditional CFD method, we need to build a large domain to contain the position of the focusing point, while in the coupled method as illustrated in Fig. 3, we only need a small CFD domain and transform CFD domain to the focusing point to get the focusing wave. Meanwhile, communication also
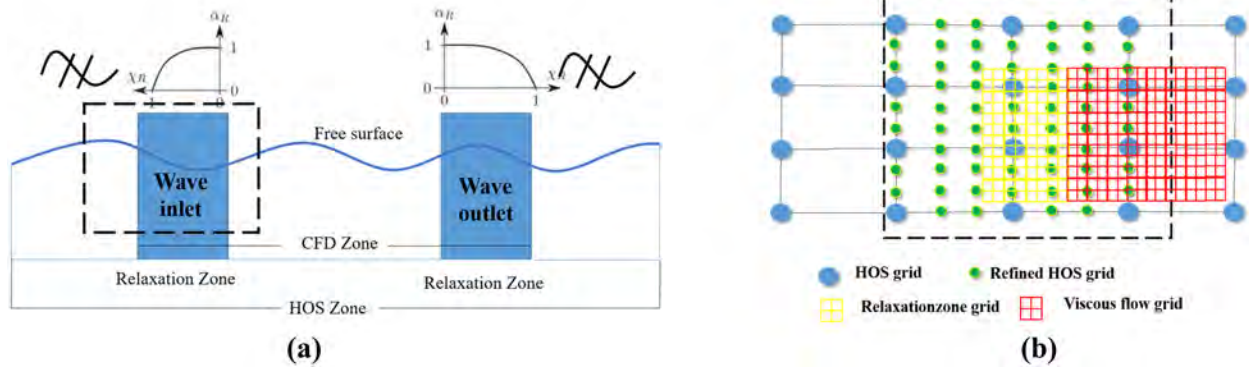
FIG. 1. The communication process of HOS solver and CFD solver: (a) the setup of HOS domain and CFD domain and (b) the communication process of HOS grid and CFD grid.
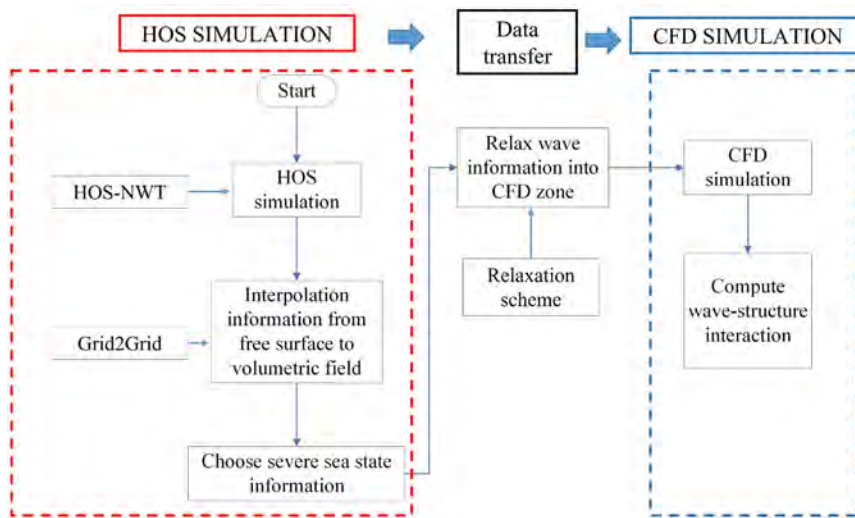

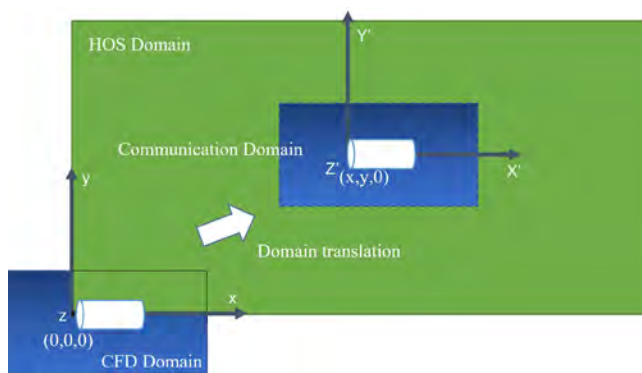FIG. 2. The calculation process of the combined solver.

FIG. 3. The correspondence of CFD domain and HOS domain.

happens in time history. We have all the flow information from HOS, including that in the time series. Therefore, we can choose desired time spot to do the simulation, which also shows an advantage in simulating focusing waves. In the coupled method, we use HOS to generate focusing wave rapidly and map the flow information around focusing time to CFD domain. In this way, we not only minimize the CFD computational domain but also reduce time in simulating focusing waves.

III. NUMERICAL TEST

A. Numerical setup

The numerical tests are chosen based on the experiments done in the Ocean Basin at Plymouth University's COAST Laboratory.[3] In this paper, we also choose this benchmark test to validate our solver and compare the results to existing experimental data and pure CFD method results. The parameters of the focusing wave is illustrated in Table I. The parameter kA stands for the wave steepness, which k is wave number ($k = \frac{2\pi}{\lambda}$) and A is wave amplitude. According to the setup of experiments, we choose the focusing point in an empty wave tank, five wave probes (WG7, WG15, WG16, WG17 and WG24) and six pressure sensors (p1, p2, p3, p4, p6, and p8) with a body in tanks. Figure 4 shows the setup of wave probes and pressure sensors in our numerical simulations. In Fig. 4(b), the pressure sensors on fixed-FPSO distribute on the semi-circle of the model, while p8, p6 and p4

TABLE I. Main parameters in test case.

CCP-WSI ID	A (m)	T_P (s)	h (m)	H_S (m)	kA	Alpha (rad)	Phi (rad)
21BT1	0.089 30	1.456	2.93	0.103	0.17	0	π

place an angle of 45° from the centerline of the FPSO. We can see that the wave probes are placed around the center of the wave tank, thus the size of CFD domain can be reduced as needed.

The physical model of experiment is a fixed-FPSO, the numerical model is built according to the experiment. The numerical model is shown in Fig. 4. The draft of the fixed-FPSO is 0.153 m. The radius of the two semi-circle parts is 0.15 m, and the total length of FPSO is 1.2 m.

B. Comparison between numerical test and experiment

As for wave generation in numerical method, it can be summarized as two types: velocity inlet wave generation and wave paddles propagation. In general, velocity inlet wave generation is commonly used for its convenience. However, when generating a focusing wave, this kind of method needs to be adjusted to simulate the correct focusing position and time point. Meanwhile, the limitation of wave maker method is when the motion of wave paddle is absent, the wave generation is impossible. Therefore, in order to improve the quality and efficiency of wave generation, a reproduction process is considered.[21–23] They used linear back transformation and Fast Fourier Transformation to handle the initial wave train spectrum; thus, they get the control signal of wave paddle by implementing Inverse Fast Fourier Transform method. By correcting amplitudes and phases in wave components from the wave train in iteration, the final results generated from the wave paddle were close to the initial one. In this paper, we applied the reproduce procedure[24] to regenerate the focusing wave with HOS-NWT, and then take the results from HOS as input information in CFD zone.

Before simulating the FPSO under the focusing wave, the method needs to be verified. The simulation is conducted in one core with total executed time 1860 s.

After obtaining the wave field from HOS, the focusing wave in CFD zone can be generated. According to the approximation solution of dispersive equation by Eckarct,[25] the wavelength can be estimated as

$$\mu = \mu_0 / \sqrt{\tanh \mu_0}, \tag{14}$$

where $\mu = 2\pi h / \lambda$, λ is wavelength and h is wave depth. $\mu_0 = (2\pi)^2 h / (gT^2)$, T is the wave period. With the known peak wave period, the wavelength is approximated to be 3.3 m. In the previous study,[26] we discussed the parameters of mesh grids, time steps as well as time integration method chosen in HOS-CFD wave generation; therefore, we applied the suitable parameters with 80 mesh grids per wavelength, 16 mesh grids per wave height and 1/800 period time steps. The total number of the grid mesh is 0.17×10^6. The time integration method applies Crank–Nicolson with a weight factor of 0.95.

Figure 5 shows the size of computational domain and mesh generation of CFD domain. The size of the CFD domain is $-7 < x < 7$ m, $-2.5 < y < 2.5$ m, $-2.95 < z < 1$ m. The computational domain displaced in Fig. 5(a) is the transformed domain, the transformation of x and y coordinates in the communication domain are chosen to be 13.886 and 10 m, respectively. The duration of the time window is chosen to be 55–70 s, therefore the actual simulation time of the coupled method is 15 s.
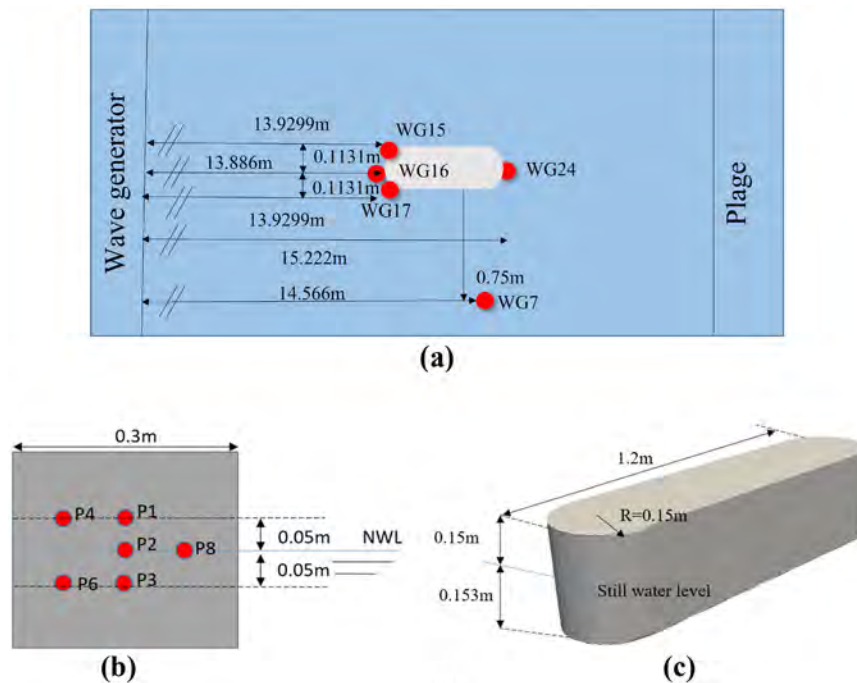
FIG. 4. The setup of numerical simulations (Ref. 3). (a) The setup of wave probes in wave tank with fixed-FPSO, (b) the setup of pressure sensors on fixed-FPSO (c) the numerical model of fixed-FPSO.
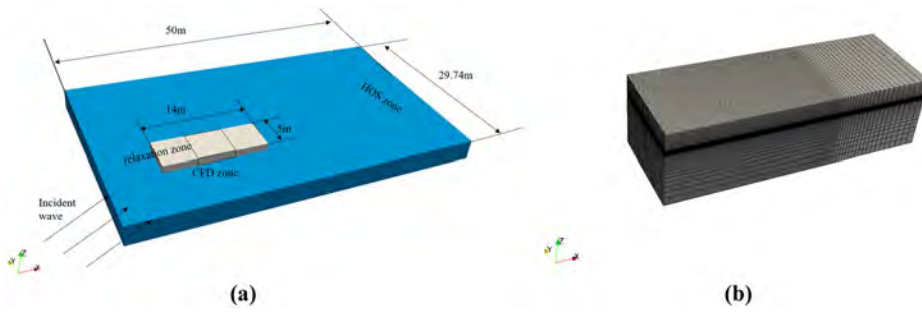
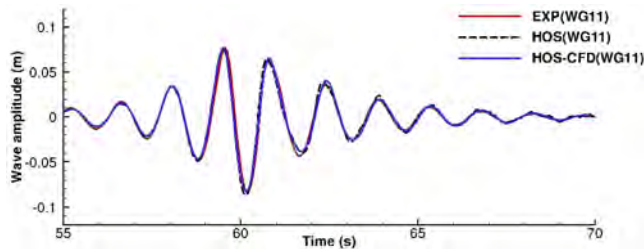**FIG. 5.** The setup of computational domain (a) and mesh generation (b).

FIG. 6. The comparison of wave elevation between the experiment and the HOS-CFD coupled method.

FIG. 7. The free surface contour in HOS-CFD coupled method in focusing time.

The comparisons between the results of numerical simulations and experimental data are shown in Fig. 6. It can be seen that the results of HOS-CFD agree well with the experimental data. An estimation of the accuracy is adopted to provide the error coefficient between the target signal and the reproduction signal,

$$R_\eta(\eta_t, \eta_r) = \frac{C(\eta_t, \eta_r)}{\sqrt{C(\eta_t, \eta_t) \cdot C(\eta_r, \eta_r)}}, \tag{15}$$

where function C is the covariance, η_t is the target surface elevation, and η_r is the reproduction surface elevation.

The correlation coefficient of numerical results and experimental data are $R_\eta = 0.98$. The result shows a good agreement between HOS results and experimental results both in amplitude and phase.

Figure 7 gives the wave counter of the free surface in the coupled method, both in HOS zone and CFD zone. The time spot of Fig. 7 is at $t = 60$ s when the wave is focused at the focusing point. It can be
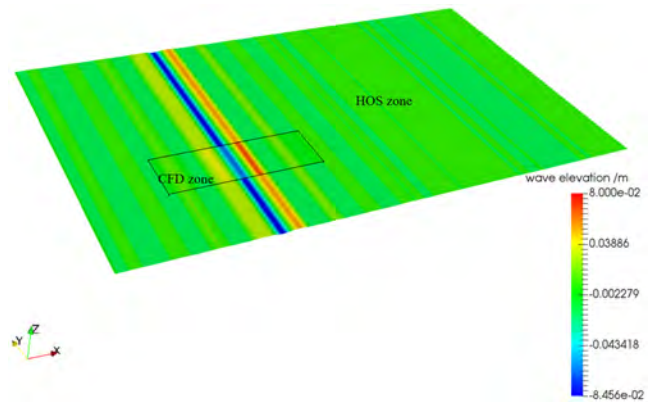
observed that the information of flow transforms well from HOS to CFD domain, showing great accuracy in combination.

After validating the focusing wave in HOS-CFD coupled method, the wave elevation around the FPSO is estimated. Before the simulations are done, a study on the size of the viscous zone is carried out. In the studies above, the wave generations are in empty tanks, thus there is no wave reflection in the viscous zone. The wave reflection only exists in relaxation zones. To avoid wave reflection in the outlet relaxation zone, we handle the mesh around the outlet relaxation zone very coarse to wipe out the wave. However, the consideration of wave reflection cannot be ignored when there is a body inside the wave tank. To give a better choice of viscous zone, three different sizes of viscous
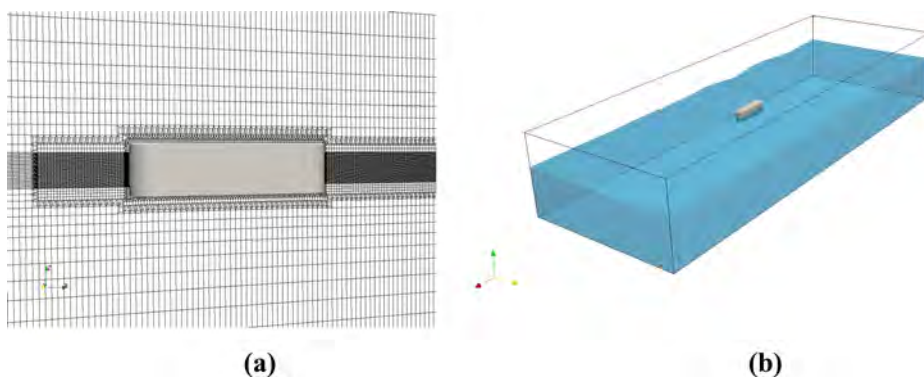

FIG. 8. The mesh grids around FPSO (a) and the computational setup (b).
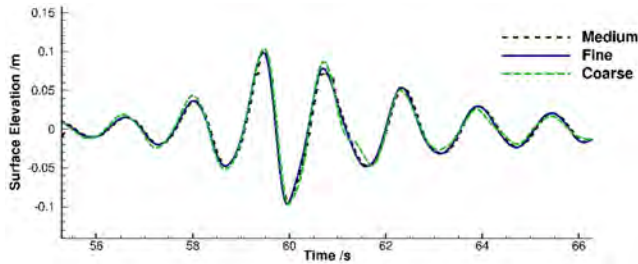
FIG. 9. The comparison of wave elevation between experiment and HOS-CFD coupled method.

zones are carried out, the results can be found in the Appendix. We finally choose the viscous zones as $-2 < x_v < 3$ m, while x_v stands for the coordinate of the viscous zone.

The mesh generation of the cases with the body in domain is shown in Fig. 8. The setup of computational domain is chosen as that in Fig. 5. To capture the wave scatter and pressure around the body, a fine grid generation is provided near the FPSO.

A mesh convergence is carried out to eliminate the influence of the numerical error from mesh grids. Three mesh generations are utilized with 0.89×10^6, 1.37×10^6, and 2.01×10^6, respectively. Naming these three mesh generations with coarse, medium, and fine, the surface elevation of scattering wave around FPSO is shown in Fig. 9. It can be seen that the results show little difference, when the mesh grids are 1.37×10^6, the value of the wave elevation tends to steady.

The scattering waves around FPSO are carried out in Fig. 10 (a). The wave probe is set in the front of the bow of FPSO. The results are compared to the experimental data. It can be seen that the numerical results agree well with the experimental results. Figure 10(b) presents the surface pressure on the FPSO. The numerical results show a fairly well agreement with the experimental results in p2.

The advantage of the coupled HOS-CFD method is not only in simulating the focusing wave accurately but also in reducing simulating time. Compared with the results we utilized CFD method before,[9] the mesh grids decrease due to the smaller CFD zone in the present method. Meanwhile, we can choose the time window of the focusing wave to reduce the time duration of simulations. We only pay attention to the time around focusing time, thus the time window before focusing time is useless. Therefore, as the CFD method need to simulate a long time to reach the focusing time, during this long-time simulation, large numerical dissipation will appear. The actual simulation time in HOS-CFD is really small, in this paper it only needs 15 s. Small simulation time brings less numerical dissipation, therefore the results will be closer to experimental results.

We apply a root mean squared (RMS) error to compare the numerical error between numerical results and experimental results on wave elevation around FPSO. The RMS error is the square root of the mean squares of the error between numerical results and experimental results. Due to the different time steps in numerical simulations and experiments, an interpolation is calculated thus bringing an additional uncertainty. The RMS error selects a time window of 55–70 s. All these RMS errors in chosen wave probes are under 0.03 m, and the wave elevation around FPSO (wave probes 15, 16 and 17) are under 0.02 m,
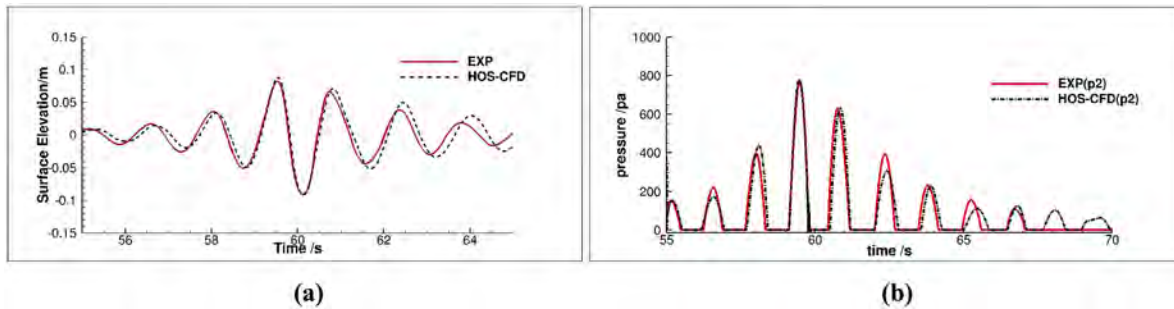

FIG. 10. The comparison of wave elevation (a) and pressure (b) between experiment and HOS-CFD coupled method.
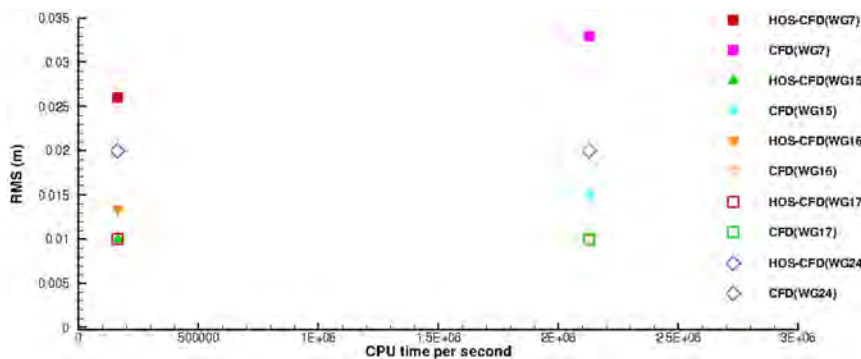

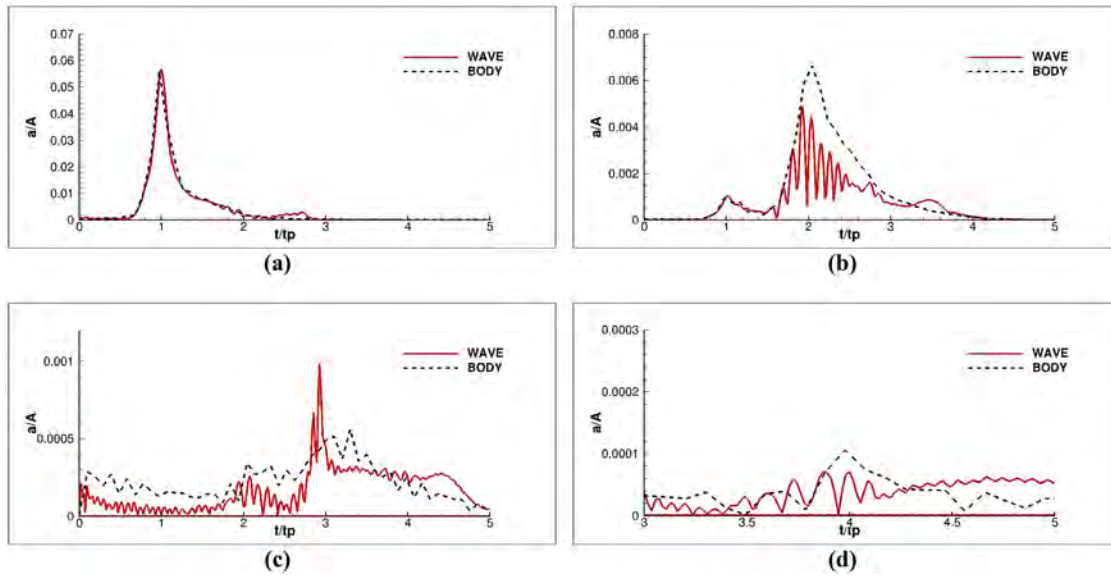**FIG. 11.** RMS in present method and CFD method of CPU time.

FIG. 12. The spectrum of harmonic components of wave elevation near the focusing point.
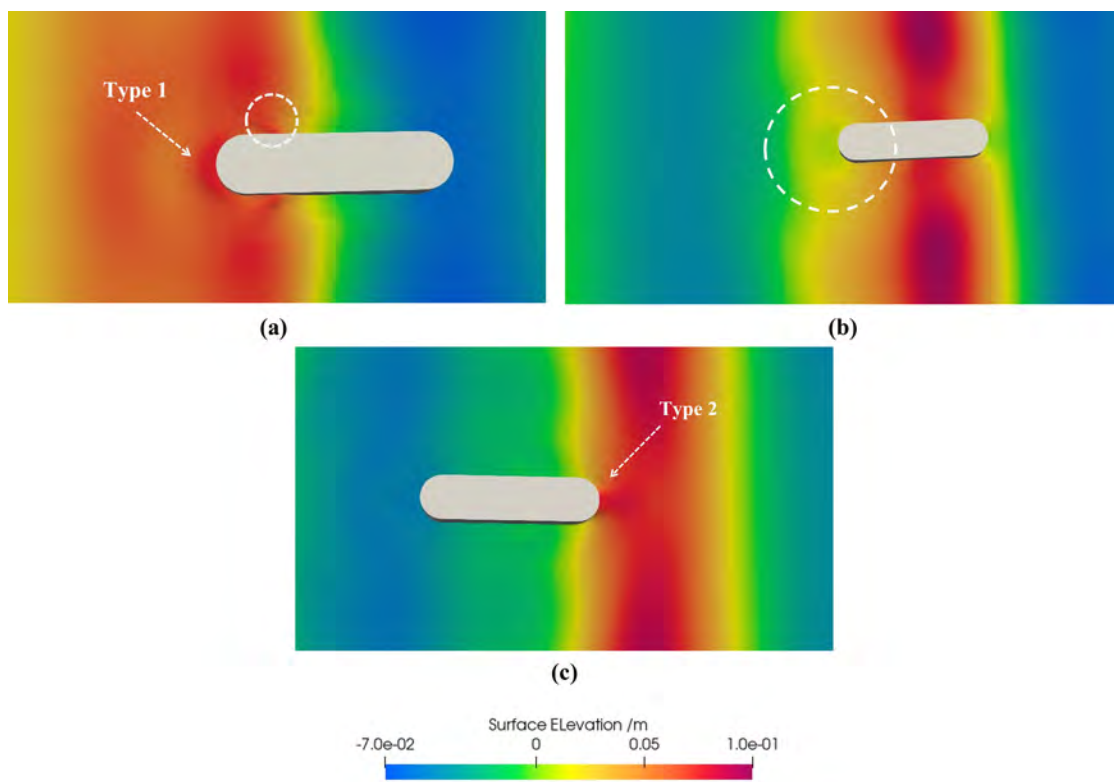

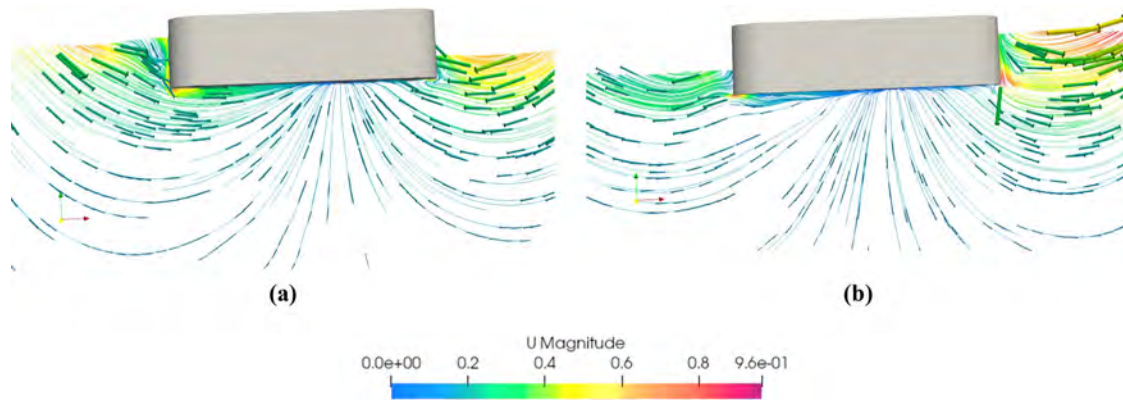**FIG. 13.** The scattering wave (a)–(c) around the model FPSO.

FIG. 14. The velocity vector [(a) type-1 and (b) type-2] around the model FPSO.

showing a good agreement. Compared to HOS-CFD and CFD methods, it can be seen that CFD method shows a better phase coincidence. To make it clear, a comparison of CPU time and RMS error is shown in Fig. 11. HOS-CFD method can reduce the CPU time to almost ten times less than CFD method.

IV. RESULTS AND DISCUSSION

A. Harmonic of scattered wave field

In order to capture the higher-harmonic components of the surface elevation, the phase-inversion method is adopted. According to the classic Stokes perturbation expansion, the incident wave group can be illustrated as[27]

$$\eta = B_{11}A\cos\theta + A^2(B_{20} + B_{22}\cos 2\theta) + A^3(B_{31}\cos\theta + B_{33}\cos 3\theta) + A^4(B_{40} + B_{42}\cos 2\theta + B_{44}\cos 4\theta) + O(A^5) \tag{16}$$

simplifying Eq. (16) with $\eta_{ij} = A^i B_{ij}\cos(j\theta)$, the higher-harmonic components can be extracted as[28]

$$(\eta^0 - H(\eta^{90}) - \eta^{180} + H(\eta^{270}))/4 = \eta_{11} + \eta_{31}, \tag{17}$$

$$(\eta^0 - \eta^{90} + \eta^{180} - \eta^{270})/4 = \eta_{22} + \eta_{42}, \tag{18}$$

$$(\eta^0 + H(\eta^{90}) - \eta^{180} - H(\eta^{270}))/4 = \eta_{33}, \tag{19}$$

$$(\eta^0 + \eta^{90} + \eta^{180} + \eta^{270})/4 = \eta_{20} + \eta_{40} + \eta_{44}, \tag{20}$$

where H is the Hilbert transforms of the signal.

Although the phase-inversion method separated the harmonic components of the surface elevation, the formulation also contains two components. Equations (17) and (18) represents first-order (i.e., linear) and second-order harmonic components, as η_{31} and η_{42} can be ignored compared to the other terms. In Eq. (20), the second-order term cannot be ignored thus the frequency is limited from 3 to 5 to eliminate the influence of this second term.
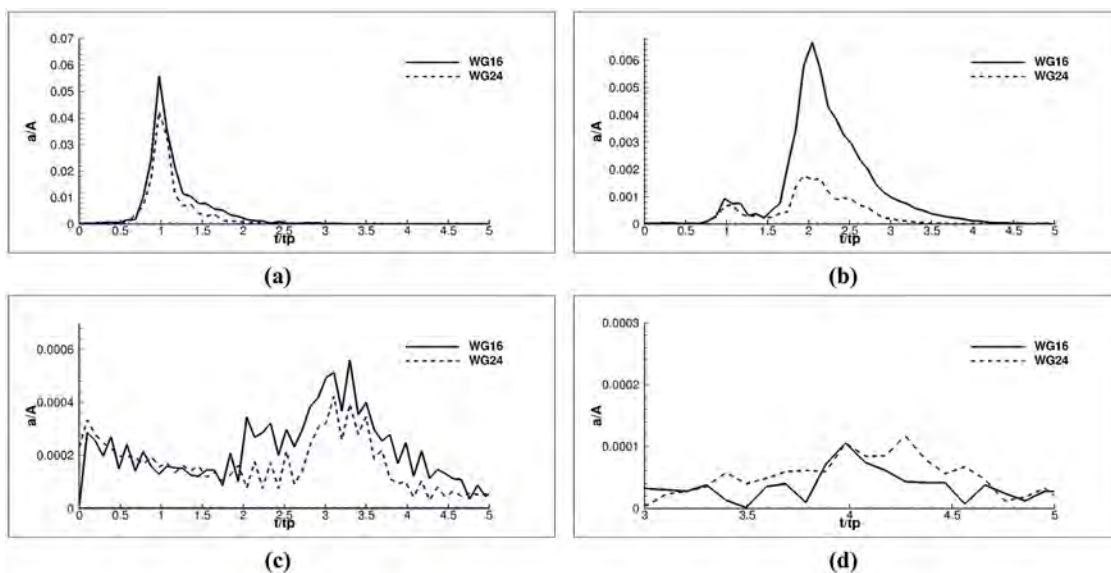

FIG. 15. The spectrum of harmonic components of wave elevation between the focusing point and the point on the stern of FPSO.
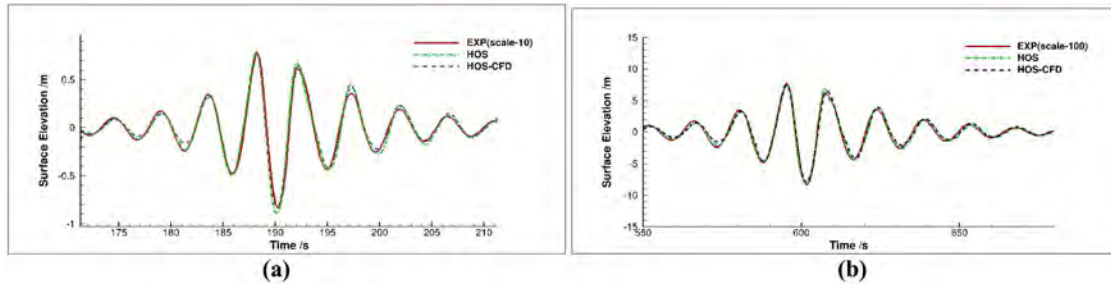
FIG. 16. The comparison of scaled wave elevation [(a) ten times scaled and (b) 100 times scaled] between scaled experiment and numerical method.

Figure 12 shows the harmonic components of wave elevation near the focusing point in the wave tank with and without a model in it. The spectrum amplitudes are dimensionless to remove the influence of wave amplitude, thus the A in Fig. 12 is the sum of the amplitude of the whole components. The existence of the model does not change the linearity of the surface elevation but magnifies the second-order and fourth-order term. Therefore, the scattering waves around the FPSO can be regarded as a nonlinear phenomenon.

The scattering wave field around the model FPSO is illustrated in Fig. 13. When the focusing wave crest approaches FPSO, a concentric scattering wave is captured, as shown in Fig. 13(a). This kind of scattering wave is considered as type-1 wave,[1] which is a radiated wave generated after the wave climbs on the body. Meanwhile, a symmetric scattering wave type is observed, shown in Fig. 13(a).

Figure 13(b) displays the fake type-2 scattering wave around the front of FPSO. type-2 wave is a symmetric scattering wave. type-2 scattering wave would appear when the anticlockwise water motion is dominant and shows higher surface elevation. However, with the existence of the rectangular shape of the body, the wave crest washes down along the rectangular shape and the wave energy does not accumulate immediately, thus the scattering wave in Fig. 13(b) does not form a real type-2 wave, but a fake one.

Another type-2 scattering wave can be observed in the downstream of the FPSO, as shown in Fig. 13(c). When the focusing wave crest leaves FPSO, the viscous in the waves drive the fluid flows along the surface of FPSO, which is the Coanda effect. This type-2 scattering wave is a smaller wave compared to type-1 scattering wave. Swan and Sheikh[1] explained the reason that this type of scattering wave had no opportunity to interact with a subsequent incident wave crest. Figure 14 illustrates the velocity vector of two specific time spot of type-1 [Fig. 13(a)] and type-2 [Fig. 13(c)].

We compared these two types with their separated components in Fig. 15. type-1 scattering wave is calculated from wave probe 16 while the type-2 scattering wave is from wave probe 24. The results is corresponding to the results from the previous research.[1] The type-2 scattering wave downstream is smaller than type-1 scattering wave both in linear and second-order harmonic components. However, when the order becomes higher, the discrepancies between these two scattering waves are smaller. In the fourth-order harmonic components, the maximum value of wave spectrum in these two types of scattering waves is almost the same.

B. Full scale simulation

After validating the method in this paper and analyzing the model-scale case, full-scale simulations are adopted. The reproduction method is utilized to reproduce scaled focusing waves. The experimental data are enlarged with a ratio of 10, thus the wave amplitude and
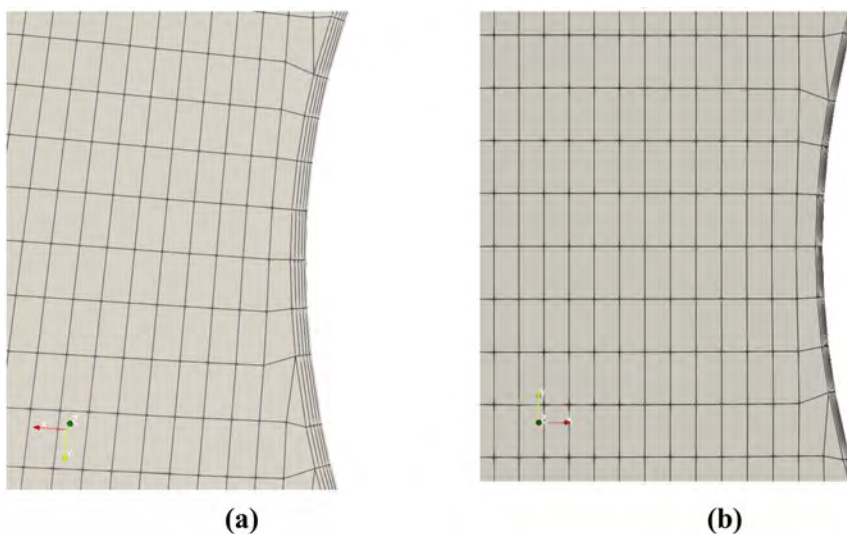

FIG. 17. The setup of boundary layer in model scale (a) and full scale (b).
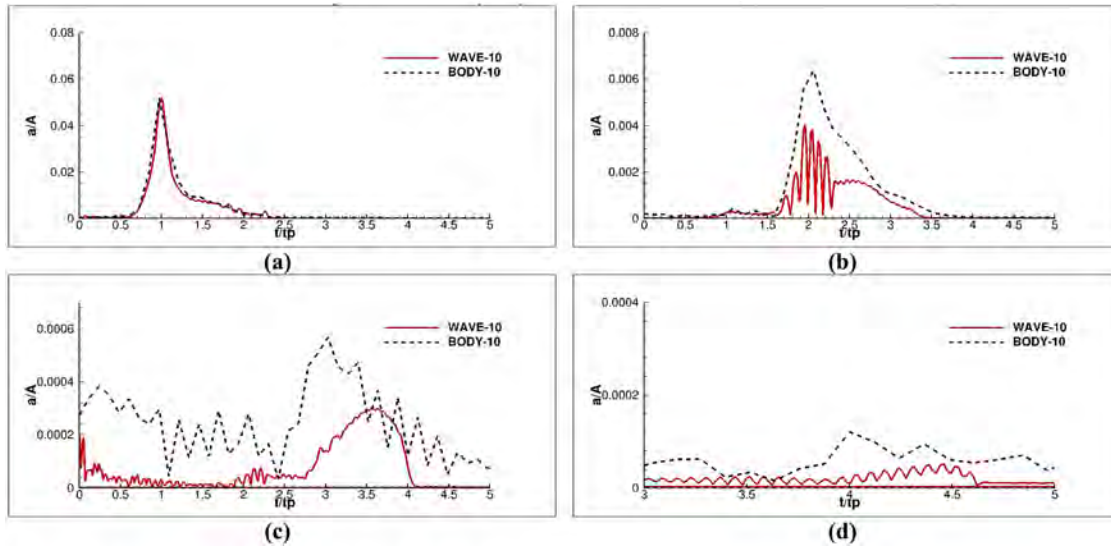
FIG. 18. The spectrum of harmonic components of scaled wave elevation near the focusing point.

wave period are enlarged with a ratio of 10 and $\sqrt{10}$, respectively. We apply the scaled experimental results to reproduce the full-scale wave fields. The scaled experimental results and numerical results are presented in Fig. 16. We adopt the same steps to simulate the 100 times scale wave fields, which are the real sea scale, as shown in Fig. 16(b). Although there exist some discrepancies between the scaled experimental data and numerical results, it can be attributed to numerical error rather than scale effect in waves.

The similarity criterion adopts the Froude number; thus, the value of viscosity in full-scale is smaller than that in model scale. The

mesh for the boundary layer at full scale is adapted to account for smaller viscous value, as shown in Fig. 17.

Figure 18 shows the harmonic components of wave elevation near the focusing point in wave tank in this ten-times scaled case. The trends of the harmonic components are similar to that in the model scale. The full-scale wave fields are utilized to simulate the focusing wave interactions with FPSO, the harmonic components of wave elevation are carried out in Fig. 19.

The scattering wave field around the full-scale FPSO is illustrated in Fig. 20. The time spot is adopted during the focusing wave crest
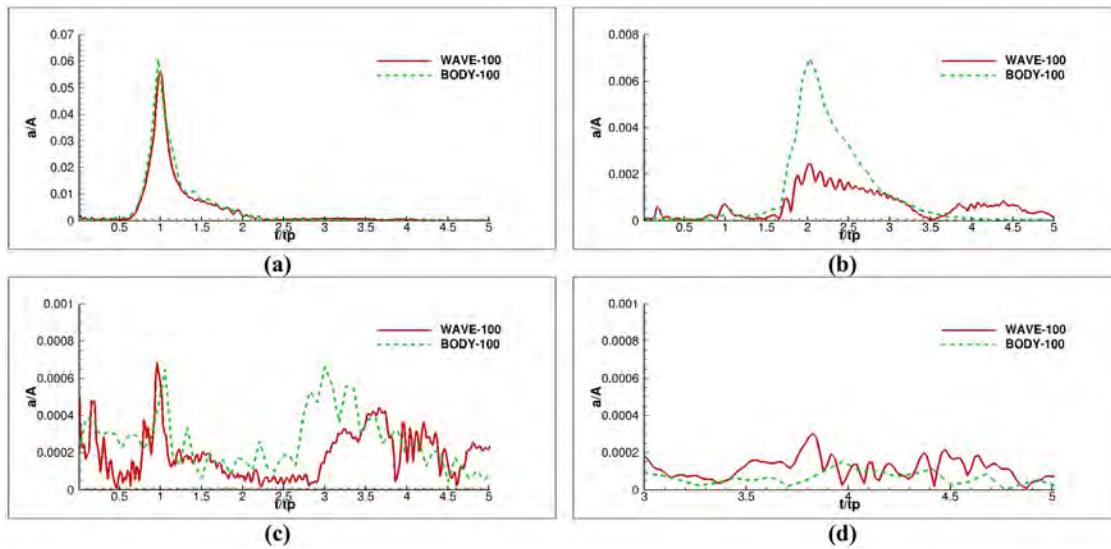

FIG. 19. The spectrum of harmonic components of full-scale wave elevation near the focusing point.
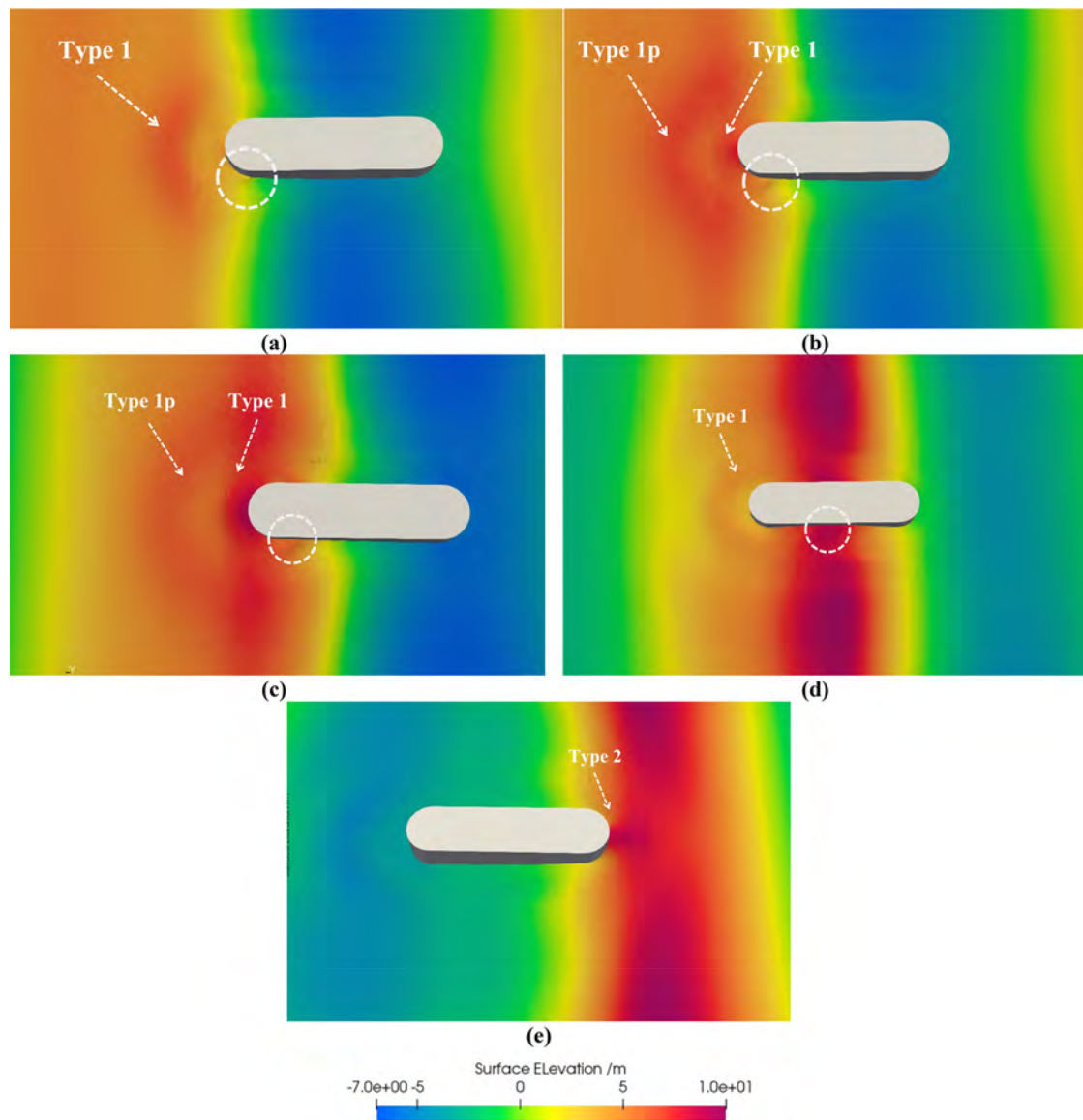
FIG. 20. The scattering wave of full scaled FPSO under steep focusing wave at (a) $t = 60.5$, (b) $t = 61.5$, (c) $t = 62.5$, (d) $t = 65.5$, and (e) $t = 70.5$.

approaches and leaves FPSO. When the wave crest approaches the FPSO, as shown in Fig. 20(a), the concentric type-1 scattering wave is observed. This kind of type-1 scattering wave is generated from the previous time step. At the same time, a small disturbance on the water surface is formed at the intersection of the semi-circle and the long section. With the wave crest passing by, a new type-1 scattering wave appears near the bow of FPSO. The disturbance on the side of FPSO moves along with the wave crest until the wave crest reaches the middle of FPSO. The type-1 scattering wave propagates in the opposite direction to the incident wave, as shown in Fig. 20(d), the newly formed type-1 wave in Fig. 20(b) becomes the "previous" type-1 wave. When the wave crest leaves FPSO, the type-2 scattering wave is

observed. Figure 21 illustrates the velocity vector of two specific time spot of type-1 [Fig. 20(c)] and type-2 [Fig. 20(e)].

In order to capture the nonlinearity clearly, a steep focusing wave is adopted. The wave frequency keeps the same but with higher wave amplitude. The steepness of the new focusing wave is 0.27. With the large wave amplitude, the green water on full-scale FPSO occurs, as shown in Fig. 22.

When the wave crest arrives at the front of FPSO, a type-1 scattering wave appears as displayed in Fig. 22(a). The second scattering wave type "type-2" is found before the green water happens. This type-2 wave appears very early and keeps the shape until the wave trough reaches. Due to the large wave energy, the propagation of type-2 is
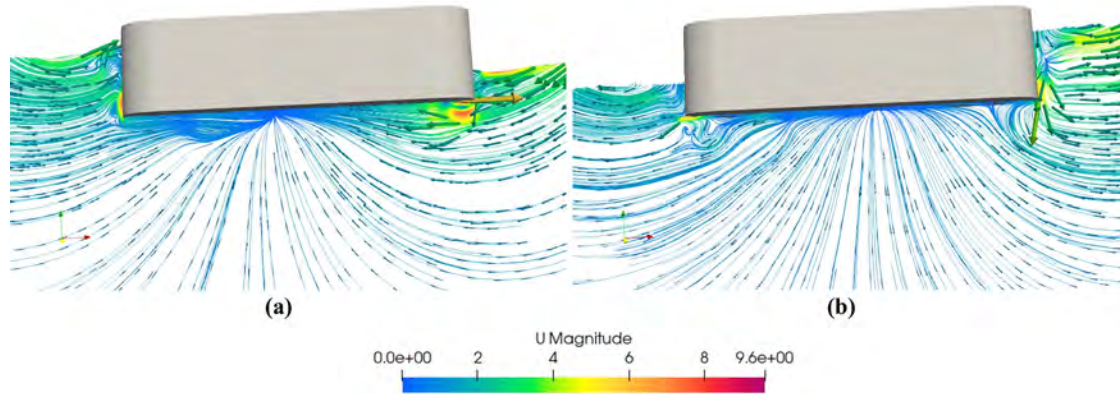
FIG. 21. The velocity vector of full scaled FPSO under steep focusing wave at (a) $t = 62.5$ and (b) $t = 70.5$.

clockwise when the wave crest passes through, and then moves anti-clockwise when the wave trough passes the FPSO. The green water shows the largest wave amplitude on the FPSO (the red color on the FPSO) and continues till the wave scattering ends. With the existence of green water, the type-1 scattering wave is rarely seen.

Figure 23 displays the vortex structure around FPSO at different time spots. The vortex identification method we adopt in this paper is "Liutex,"[29] which defined the rotation part of the vorticity and can represent the direction and magnitude of the rotational motion. When the type-1 scattering wave is observed, a vortex ring appears in the front of FPSO. With the propagation of wave crest, part of the energy in scattering waves transfers from "type-1" vortex to type-2 vortex, and forms vortex bunches around the lower edge of FPSO. The rest of energy from type-1 vortex propagates oppositely, forming the previous type-1 vortex. However, with the existence of the green water, the previous type-1 vortex vanishes rapidly. The type-2 vortex accumulates and finally merges in the front of FPSO, as shown in Fig. 23(e).

C. Scale effect

In this section, the scale effects among the different scaling ratios are discussed. Figure 24 presents the comparison of surface elevation around FPSO near the focusing point among these three scaled cases with $kA = 0.17$. The ten-scaled case and real scaled case are limited to suit the model case. Although the shape of the curve shows little changes, the amplitude and curvature of the scaled cases shows different from that in the model scaled case. In order to make it clear, the harmonic components are compared among these three cases, as illustrated in Fig. 25.

All the harmonic components are displayed in Fig. 25. The scale effects not only appear on linear components but also in higher-order harmonic components. However, the differences in second-order harmonic components are not proportional to the scale factor. The increase in maximum value in each order component compared to the model case is listed in Table II.

It can be seen that the largest increase appears in the third-order at the full-scale case. The increments of linear and second-order components in scaled cases are almost the same and present a two times growth rate. The increment in fourth-order components is smaller than that in third-order components, while the value in forth-order of

the full-scale case is still significant. We can indicate that with the increase in the scale, the linear and second-order components will increase at a twice growth rate. In the large scale or real-scale cases, the scattering wave shows a higher (third or more) order harmonic situation.

Figure 26 illustrates the harmonic components of scattering waves around FPSO stern (WG24) among these three scaled cases. On the contrary to the harmonic components around the front of FPSO, the scattering wave of the full-scale case decreases in linear and higher-order harmonic components. The increase in maximum value in each order component compared to the model case is listed in Table III. The dimensionless harmonic components in full-scale case are smaller than that in model scaled case, the closest value to the model case appears in the second-order harmonic components. The ten-scale case exhibits great increment in second- and third-order harmonic components. We indicate that the influence of wave amplitude dominates the full-scale case. The nonlinearity of the scattering wave around FPSO stern (which is type-2 wave) does not increase with the wave amplitude and body size. The nonlinearity dissipates along the large size of the FPSO. However, in the ten-scaled case, the nonlinearity dominates the scattering wave in type-2 wave.

To give a clearer view of the type-1 and type-2 scattering waves, a vorticity colored by the velocity is carried out. Figures 27 and 28 present the vorticity around the FPSO in three cases. The time spot chooses when the focusing wave approaches and leaves the FPSO. The view of vorticity displays the concentric fields in the front of FPSO, while symmetric fields in the stern of FPSO. Since the scattering waves are almost the same around the model- and full-scale FPSO (shown in Figs. 14 and 20), it can be assumed that the types of scattering waves reveal the second-order harmonic components in flow fields.

Figure 29 presents the vortex around the FPSO in model- and full-scale cases. The time spot chooses when the focusing wave arrives and leaves the FPSO. It can be seen that there are two vortices around the front of FPSO both in model- and full-scale cases. The vortex ring around the free surface will spread in opposition to the incident wave, while the vortex ring around the edge of FPSO will transfer energy to form type-2 vortex. However, as we mentioned before, the type-2 scattering wave only appears in the stern of FPSO, thus the type-2 vortex will disappear. With the propagation of wave crest, the vortex bunch
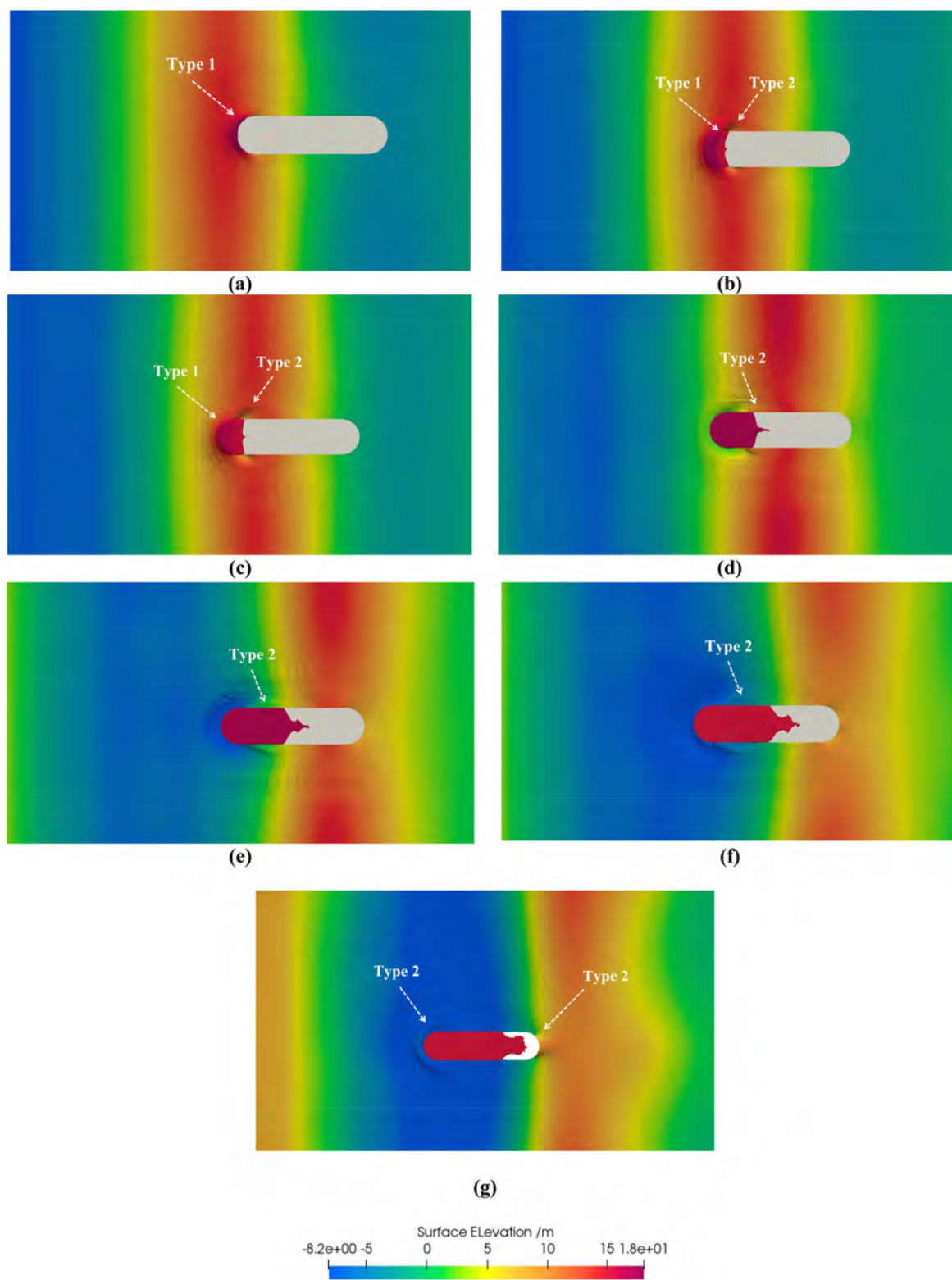
FIG. 22. The scattering wave of full scaled FPSO at (a) t = 50.5 s, (b) t = 52 s, (c) t = 53 s, (d) t = 55 s, (e) t = 55.5 s, (f) t = 56.5 s, and (g) t = 58 s.
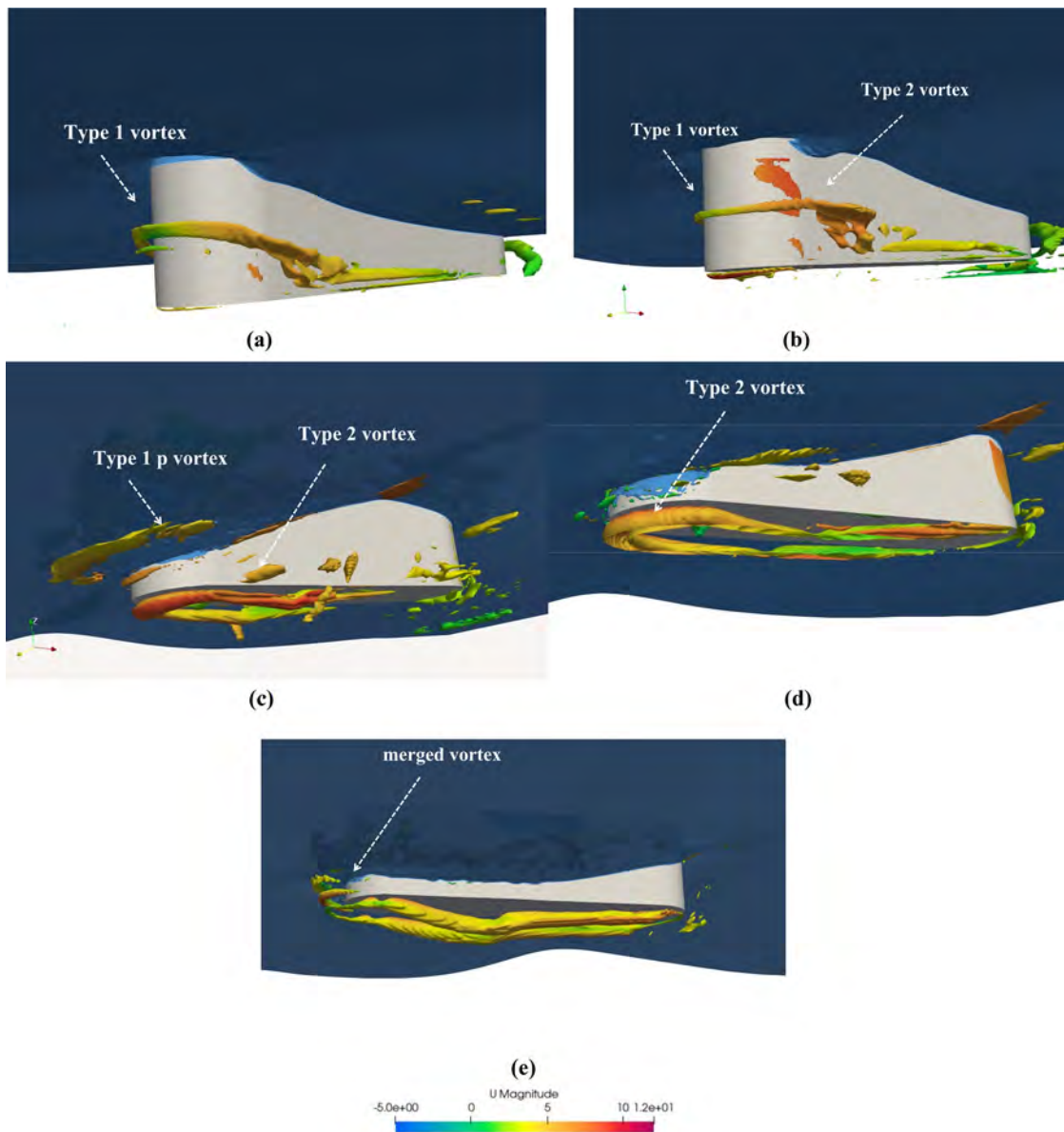
10 October 2023 15:01:28

FIG. 23. The vortex structure of full scaled FPSO at (a) t = 50.5 s, (b) t = 52 s, (c) t = 55.5 s, (d) t = 56.5 s, and (e) t = 58 s.
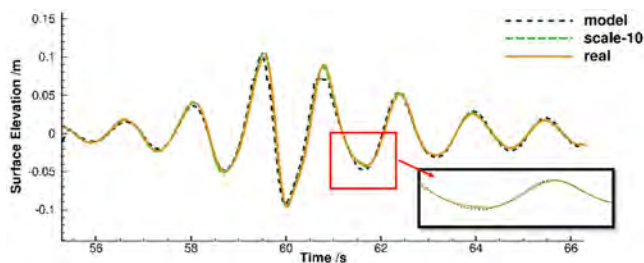

FIG. 24. The comparison of surface elevation among model scaled case, ten-scaled case, and full-scaled case.

can be observed under the edge of FPSO. The vortex bunch in full-scale case extends from the bow to the stern of FPSO. When the wave crest leaves FPSO, a type-2 scattering wave can be observed. Therefore, the type-2 scattering wave forms a V-shaped vortex, as shown in Figs. 29(c) and 29(d).

Except for those apparent vortices mentioned above, there exists different vortices between model- and full-scale cases. In Figs. 29(b) and 29(c), a complete vortex bunch can be considered. It can be suggested that the complete vortex bunch dominates the third- or higher-order of components.

To study the nonlinearity in the case of $kA = 0.27$, another flow field analysis method should be provided. The phase-separation
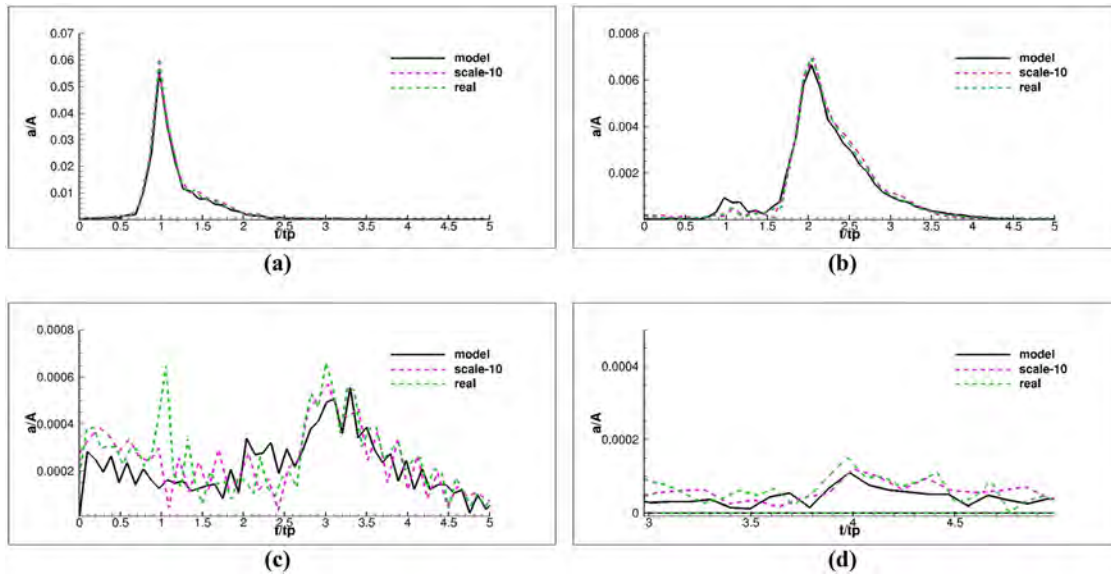
FIG. 25. The scale effects of spectrum of harmonic components of wave elevation near the focusing point.

TABLE II. Increase of maximum value in each order in scaled cases near focusing point.

Order	Linear	Second-order	Third-order	Fourth-order
Ten-scale	7.54%	6.83%	29.96%	2.56%
Full-scale	15.09%	11.11%	41.56%	24.79%

method cannot deal with breaking waves or green water. We adopt DMD (dynamic mode decomposition)[30] method to extract dynamic information from the flow fields. We apply the snapshots of Q in the surface panel as input data, and the dimension is reduced to one dimension. Figure 30 gives the proportion of energies in each dynamic mode in the model- and full-scale. It can be seen that the distribution of energy is concentrated in the first and second modes in the model-scale, and the energies of other modes are rarely small. In the full-scale
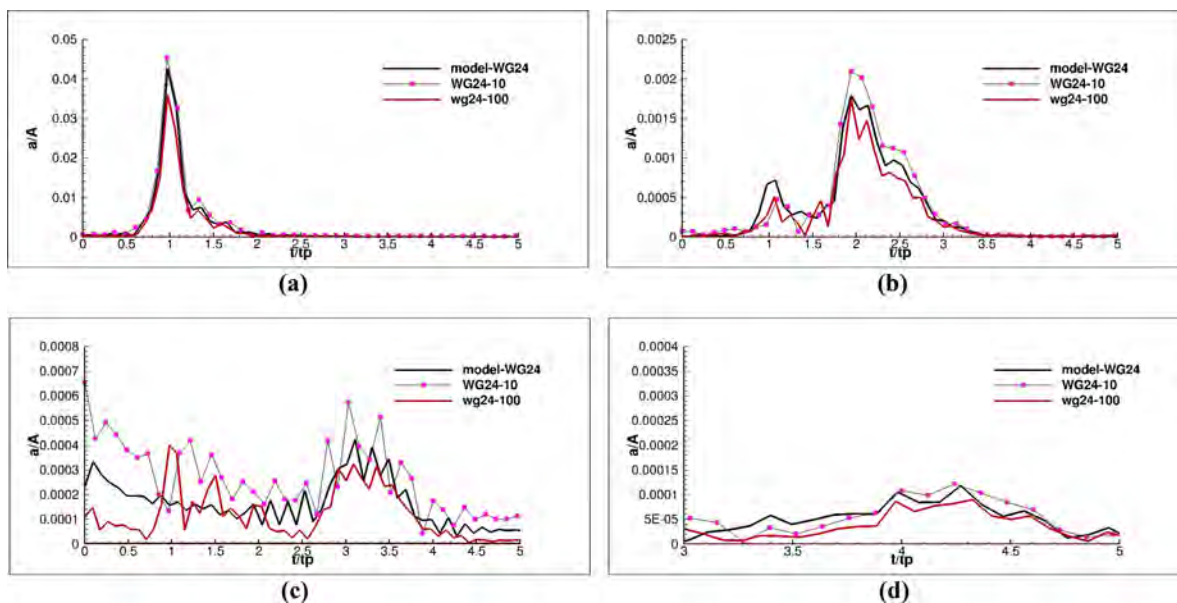

FIG. 26. The scale effects of spectrum of harmonic components of wave elevation near the stern of the FPSO.

TABLE III. Increase of maximum value in each order in scaled cases near the stern of FPSO.

Order	Linear	Second-order	Third-order	Fourth-order
Ten-scale	0.5%	11.47%	55.90%	0.56%
Full-scale	−20.6%	−8.57%	−23.1%	−25.4%

case, the distribution of energy is concentrated in the first three modes, and the energies in other modes are close to zero.

The vortex around model-scaled FPSO is given in Fig. 31. The time spot is chosen the same as in Figs. 23(a) and 23(e). Compared to the type-1 vortex around full-scaled FPSO, the vortex around model-scaled FPSO is discontinuous. There exists another small vortex on the surface of FPSO. This small vortex on the surface may contribute to the energy in higher-order modes such as fourth or fifth modes. When the wave crest leaves the body, a complete vortex bunch is observed under the edge. The vortex also accumulates in the front of the FPSO, but is smaller than that around full-scaled FPSO. There are three kinds of vortex "ring" around full-scale FPSO [shown in Fig. 23(e)], the vortex ring near the free surface may dominate the energy in the third mode.

V. CONCLUSIONS

In this paper, the nonlinearity in scattering waves around a fixed-FPSO in model- and full-scale under focusing waves is discussed. The numerical method adopts potential solver high-order spectral method (HOS) combined with viscous solver naoe-FOAM-SJTU. Taking HOS fields as initial flow fields, the whole wave field can be predicted and the severe condition can be chosen. Thus the CFD domain simulation can reduce its time-consuming. The HOS-CFD coupled method has the ability in solving large-scale structures in real-state focusing waves in an accurate and efficient way. The combined method is verified through the benchmark test, with a reproduce procedure adopted to regenerate accurate focusing waves. The comparison between numerical results and experimental data shows a good agreement, giving accuracy and stability of the present method. In addition, the RMS error and CPU time of the present numerical method and CFD method are compared, showing the present method a better solution in reducing computational time. Considering non-breaking and green water conditions, two kinds of flow analysis methods are utilized to study the nonlinearity in the scattering waves both in model and full-scale cases. A phase-separation method and a DMD method are utilized to study the harmonic components of the scattering waves.
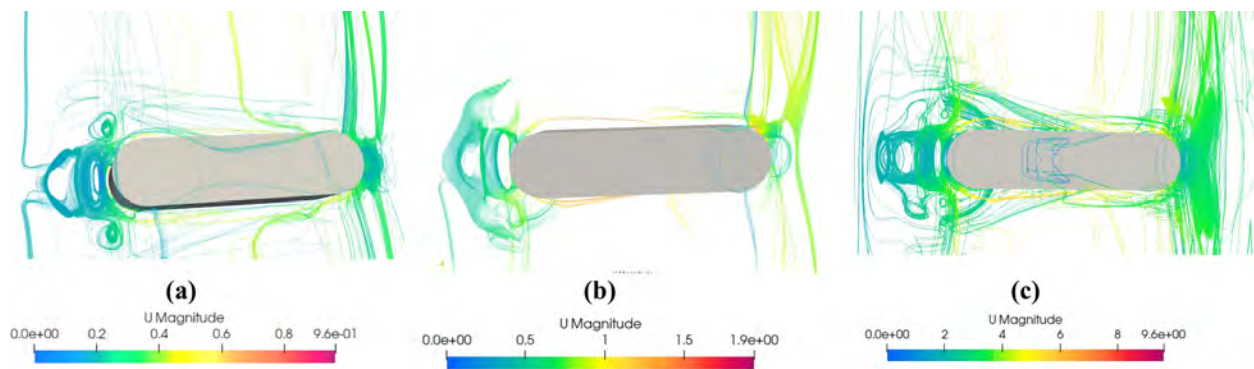

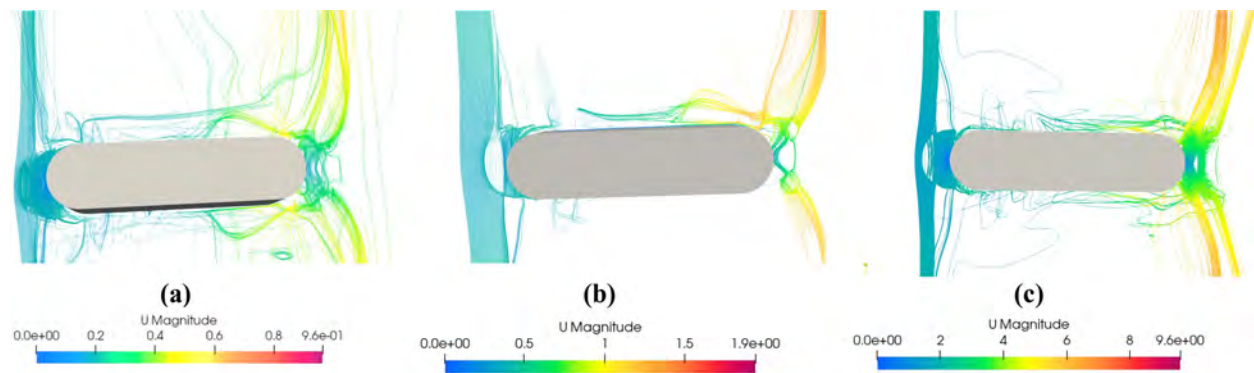**FIG. 27.** The vorticity of model scale (a), ten-scaled case (b) and full-scaled case (d) on the bow of FPSO.

FIG. 28. The vorticity of model scale (a), ten-scaled case (b) and full-scaled case (d) on the stern of FPSO.
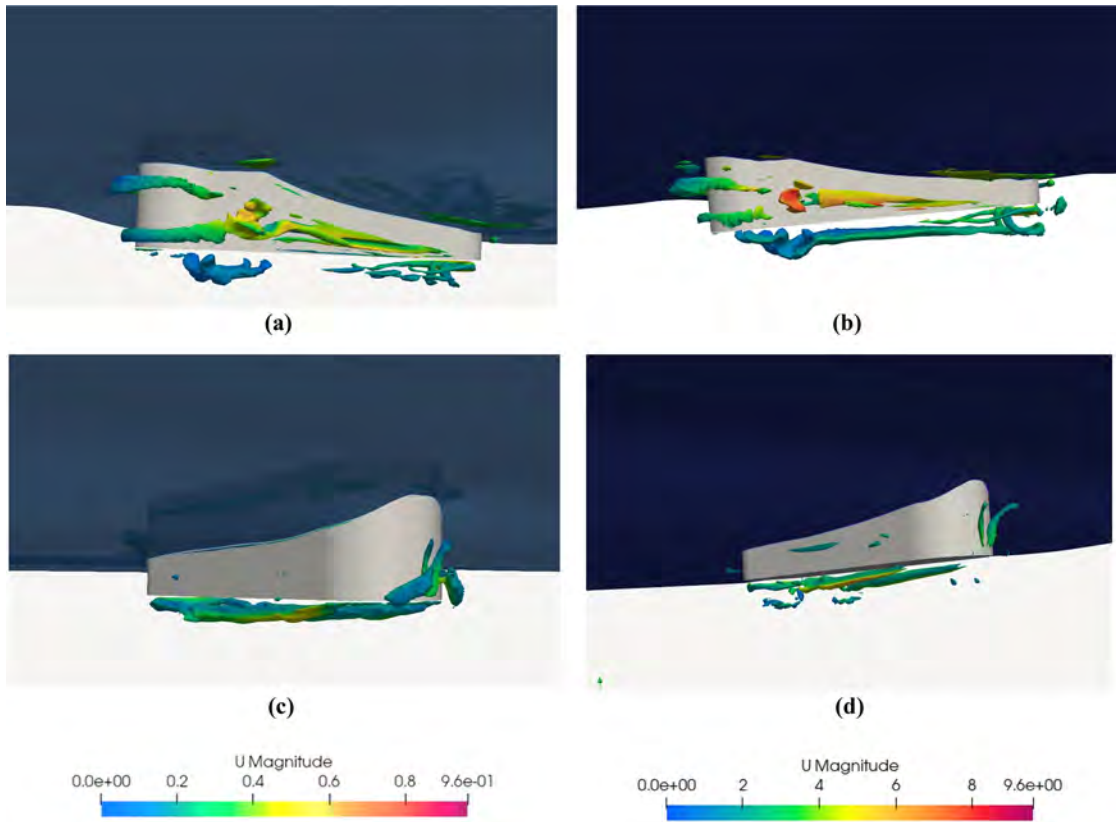
FIG. 29. The vortex of FPSO in model case [(a) type-1 and (c) type-2] and in full scale case [(b) type-1 and (d) type-2].

Two kinds of wave steepness are considered in simulating full-scaled FPSO under focusing waves. The scattering waves around the FPSO can be considered as the higher-order harmonic components. In the $kA = 0.17$, the type-1 scattering wave is observed in the front of FPSO, and the type-2 scattering wave only appears in the rear of FPSO. The type-2 scattering wave is a small scattering wave, which reveals smaller linear and second-order harmonic components compared to that in type-1 scattering wave. In the $kA = 0.27$, the type-2
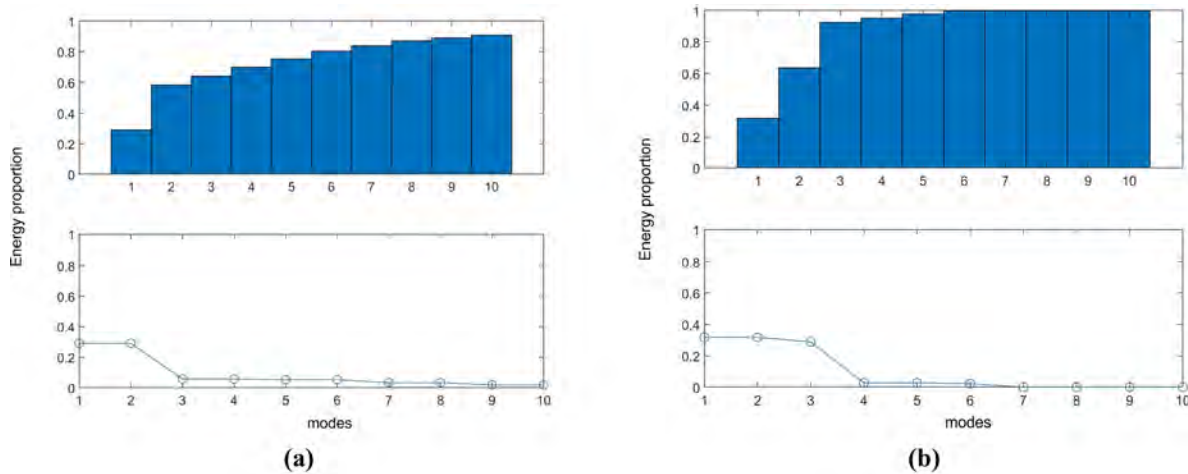

FIG. 30. The proportion of energy in each dynamic modes in model case (a) and in full scale case (b).
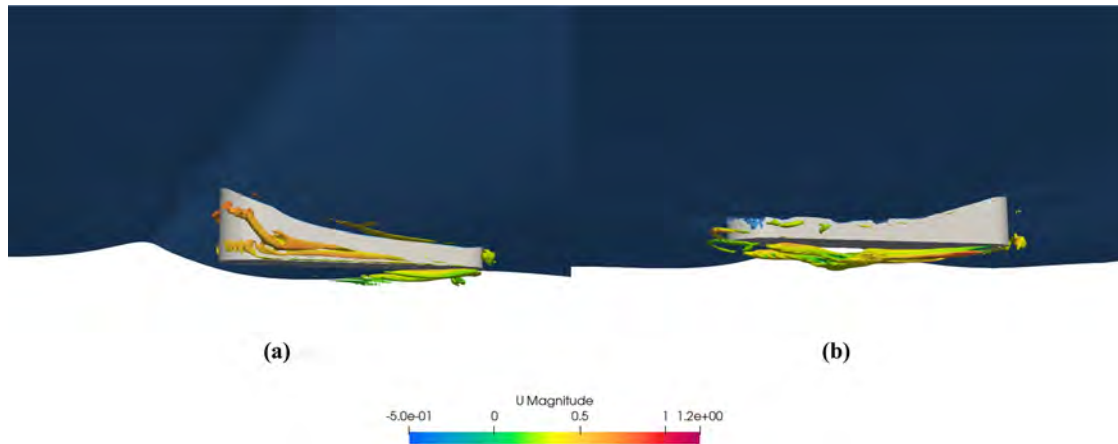
FIG. 31. The vortex of FPSO in model case [(a) near the focusing point and (b) around stern of FPSO].

scattering wave can be observed at the side of FPSO. The vortex around the body is relevant to these scattering waves. The type-1 vortex presents like a ring, the upper ring propagates in the opposite direction, and the lower one transfer the energy to form type-2 vortex. However, due to the long side of the FPSO, the energy becomes the vortex bunch and forms a type-2 vortex in the rear of FPSO. This kind of type-2 vortex presents a "V" shape.

Cases with the scale ratio of 10 and 100 (full-scale) times of model and wave are considered. The scale effect of scattering wave is significant in third-harmonic components in the front of FPSO in full-scale case and in the rear of FPSO in ten-scale case. When the focusing wave approaches FPSO, the linear and second-order components tend to grow in twice the value as the scale increases. When the focusing wave leaves FPSO, the wave energy of full-scale case dominates the scattering wave, presenting a smaller harmonic component. The types of scattering waves reveal the second-order harmonic components, while the vortex bunch may contribute to third or higher-order harmonic components in the flow fields. In the larger wave steepness case, the energy in flow field around full-scale FPSO is concentrated in the first three modes while in model-scale is concentrated in the first two modes. The full-scale case in two different wave steepness shows higher-order characteristics in the flow field.

This paper applies a coupled method to reveal its advantage in simulating the full-scale wave-structure interaction. The high-order harmonic components as well as the vortex around the FPSO in different scale ratios of test model are considered. The type of scattering waves in different scale ratios shows little difference, while large-scale cases present larger values in three- or fourth-order harmonic components. As those higher-order harmonic components may bring dangerous structure responses, the scale effects need to be considered in those focusing or steep waves.

AUTHOR DECLARATIONS
Conflict of Interest

The authors have no conflicts to disclose.

Author Contributions

Yuan Zhuang: Conceptualization (equal); Data curation (equal); Formal analysis (equal); Investigation (equal); Methodology (equal); Resources (equal); Validation (equal); Visualization (equal); Writing – original draft (lead). **Weiwen Zhao:** Conceptualization (equal); Data curation (equal); Formal analysis (equal); Investigation (equal); Validation (equal); Visualization (equal); Writing – review & editing (equal). **Decheng Wan:** Conceptualization (lead); Funding acquisition (lead); Investigation (equal); Methodology (equal); Resources (equal); Supervision (lead); Validation (equal); Writing – review & editing (lead).

DATA AVAILABILITY

The data that support the findings of this study are available from the corresponding author upon reasonable request.

APPENDIX: THE PARAMETRIC AND CONVERGENCE STUDY

Before the simulations are taken, a parametric study of HOS order is carried out. For the nonlinear wave generation, Ducrozet
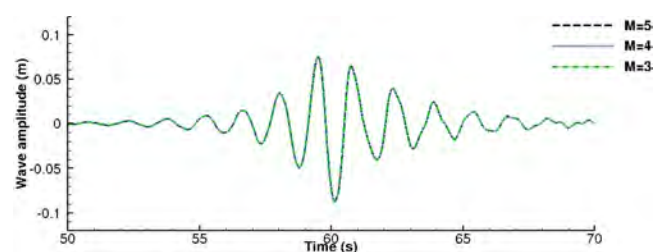

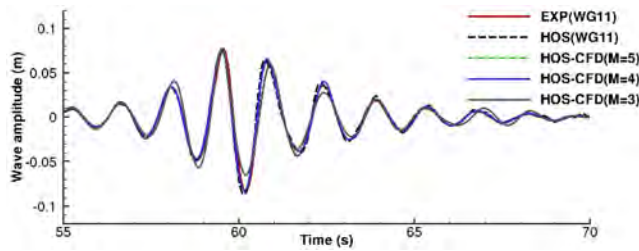**FIG. 32.** The parametric study of HOS order.

FIG. 33. The time history of wave elevation in different HOS-order of HOS-CFD coupled method.
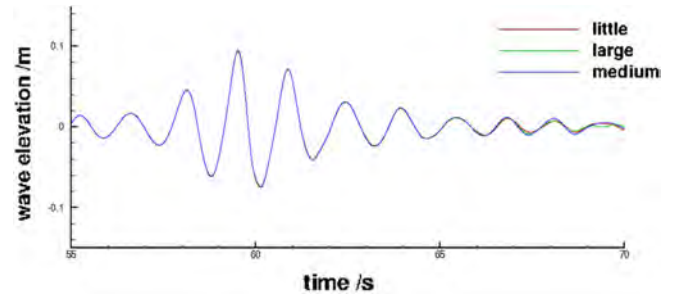

FIG. 34. The time history of wave elevation in different viscous zones.
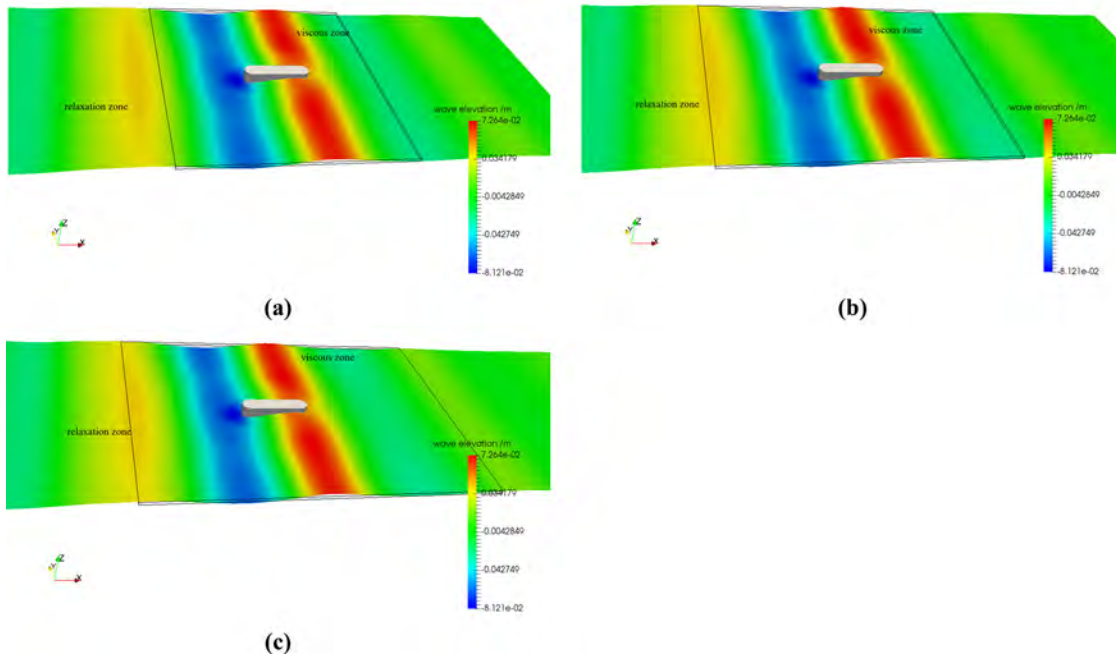

FIG. 35. The wave field around the body in focusing time in different sizes of viscous zone, (a) short viscous zone, (b) medium viscous zone and (c) large viscous zone.

et al.[17] recommended to choose the order of 3, 4 or 5 to make certain that the wave generation can capture the nonlinearity. As for the unidirectional nonlinear wave, the HOS order of 3, 4 or 5 seems has little influence on the wave elevation, shown in Fig. 32. However, when we considered HOS-CFD coupled method, with small HOS order, some nonlinear features are lost during the coupling process. It can be seen in Fig. 33, HOS order with 4 or 5 will be better to capture the nonlinearity in HOS-CFD coupled method.

Figure 34 shows the time history of wave elevation in different viscous zones. It can be seen that the length of viscous zones does not much influence the wave elevation around the structure. In order to give a clear view of wave fields around the fixed-FPSO, Fig. 35 illustrates the wave fields around the body in different viscous zones in the focusing time. The wave fields explain the same curves of these three conditions, for the wave scatter around the body is all included even in the small viscous zone. However, we can find that about four periods after the focusing time, large viscous zone and short viscous zone presents a smaller wave amplitude. The smaller wave amplitude in large viscous zone may due to numerical dissipation for the larger computational domain, the phenomenon in small viscous zone may due to the wave reflection. Although the small viscous zone does not affect the wave elevation around the focusing time, we still choose medium viscous zone in the case of wave reflection.

REFERENCES

[1]C. Swan and R. Sheikh, "The interaction between steep waves and a surface-piercing column," Philos. Trans. R. Soc. A **373**(2033), 20140114 (2015).

[2]O. M. Faltinsen, "Hydrodynamics of marine and offshore structures," J. Hydrodyn. **26**(6), 835–847 (2014).

[3]T. Mai, D. Greaves, A. Raby, and P. H. Taylor, "Physical modelling of wave scattering around fixed FPSO-shaped bodies," Appl. Ocean Res. **61**, 115–129 (2016).

[4]H. Chen, L. Qian, and D. Cao, "Harmonic structure of the nonlinear force on a fixed ship-shaped floating production, storage and offloading vessel under dispersive phase-focused wave groups," Phys. Fluids **35**(4), 042103 (2023).

[5]S. Huo, S. Deng, Z. Song, W. Zhao, and D. Wan, "On the hydrodynamic response and slamming impact of a cylindrical FPSO in combined wave-current flows," Ocean Eng. **275**, 114139 (2023).

[6]J. R. Chaplin, "On frequency-focusing unidirectional waves," Int. J. Offshore Polar Eng. **6**(02), 131–137 (1996).

[7]A. P. Engsig-Karup and C. Eskilsson, "Spectral element FNPF simulation of focused wave groups impacting a fixed FPSO," in *Proceedings of the 28th International Ocean Polar Engineering Conference*, Sapporo, Japan (ISOPE, 2018), Vol. 1, pp. 1443–1450.

[8]Z. Xie, S. Yan, Q. Ma, and T. Stoesser, "Numerical modelling of focusing wave impact on a fixed offshore structure," in *Proceedings of the 28th International Ocean Polar Engineering Conference*, Sapporo, Japan (ISOPE, 2018), Vol. 1, pp. 1451–1457.

[9]Y. Zhuang and D. C. Wan, "Numerical study of focused waves acting on a fixed FPSO-shaped body," Int. J. Offshore Polar Eng. **29**(2), 128–140 (2019).

[10]Q. Li, S. Yan, J. Wang, and Q. Ma, "Numerical simulation of focusing wave interaction with FPSO-like structure using FNPT-NS solver," in *Proceedings of the 28th International Ocean Polar Engineering Conference*, Sapporo, Japan (ISOPE, 2018), Vol. 1, pp. 1458–1464.

[11]P. Higuera, E. Buldakov, and D. Stagonas, "Numerical modelling of wave interaction with an FPSO using a combination of OpenFOAM and Lagrangian models," in *Proceedings of the 28th International Ocean Polar Engineering Conference*, Sapporo, Japan (ISOPE, 2018), Vol. 1, pp. 1486–1491.

[12]I. Gatin, H. Jasak, V. Vukcevic, and S. Downie, "Focused wave loading on a fixed FPSO using naval hydro pack," in *Proceedings of the 28th International Ocean Polar Engineering Conference*, Sapporo, Japan (ISOPE, 2018), Vol. 1, pp. 1434–1442.

[13]D. Dommermuth and D. Yue, "A high-order spectral method for the study of nonlinear gravity waves," J. Fluid Mech. **184**, 267–288 (1987).

[14]J. Wang, W. Zhao, and D. C. Wan, "Development of naoe-FOAM-SJTU solver based on OpenFOAM for marine hydrodynamics," J. Hydrodyn. **31**(1), 1–20 (2019).

[15]E. J. Ransley, S. Yan, S. A. Brown, Y. Zhuang, and D. Wan, "A blind comparative study of focused wave interactions with a fixed FPSO-like structure (CCP-WSI blind test series 1)," Int. J. Offshore Polar Eng. **29**(2), 113–127 (2019).

[16]R. I. Issa, "Solution of the implicitly discretised fluid flow equations by operator-splitting," J. Comput. Phys. **62**(1), 40–65 (1986).

[17]G. Ducrozet, F. Bonnefoy, D. Le Touzé, and P. Ferrant, "Implementation and validation of nonlinear wavemaker models in a HOS numerical wave tank," Int. J. Offshore Polar Eng. **16**(03), 161–167 (2006).

[18]N. G. Jacobsen, D. R. Fuhrman, and J. Fredsùe, "A wave generation toolbox for the open-source CFD library: OpenFoam®," Int. J. Numer. Methods Fluids **70**(9), 1073–1088 (2012).

[19]Y. M. Choi, M. Gouin, G. Ducrozet, B. Bouscasse, and P. Ferrant, "Grid2Grid: HOS wrapper program for CFD solvers," arXiv:1801.00026 (2017).

[20]Y. Zhuang, D. C. Wan, B. Bouscasse, and P. Ferrant, "Regular and irregular wave generation in OpenFOAM using high order spectral method," in *Proceedings of the 13th OpenFOAM Workshop (OFW)*, Shanghai (OFW13, 2018), pp. 189–192.

[21]K. Daemrich, W. Eggert, and S. Kohlhase, "Investigations on irregular waves in hydraulic models," Coastal Eng. **1**(17), 186–203 (1980).

[22]H. Fernandez, S. Schimmels, and V. Sriram, "Focused wave generation by means of a self-correcting method," in *Proceedings of the 23rd International Offshore and Polar Engineering Conference (ISOPE)*, Anchorage (ISOPE, 2013), Vol. 3, pp. 917–924.

[23]Q. W. Ma, S. Yan, D. Greaves, T. Mai, and A. Raby, "Numerical and experimental studies of interaction between FPSO and focusing waves," in *Proceedings of the International Ocean and Polar Engineering Conference* (ISOPE, 2015), pp. 655–662.

[24]G. Ducrozet, F. Bonnefoy, and P. Ferrant, "On the equivalence of unidirectional rogue waves detected in periodic simulations and reproduced in numerical wave tanks," Ocean Eng. **117**, 346–358 (2016).

[25]C. Eckart, "The propagation of gravity waves from deep to shallow water," *Gravity Waves: Proceedings of NBS Semicentennial Symposium on Gravity Waves* (1952), p. 165.

[26]Y. Zhuang and D. C. Wan, "Parametric study of a new HOS-CFD coupling method," J. Hydrodyn. **33**(1), 43–54 (2021).

[27]J. D. Fenton, "A fifth-order Stokes theory for steady waves," J. Waterw. Port Coastal Ocean Eng. **111**(2), 216–234 (1985).

[28]C. J. Fitzgerald, P. H. Taylor, R. E. Taylor, J. Grice, and J. Zang, "Phase manipulation and the harmonic components of ringing forces on a surface-piercing column," Proc. R. Soc. A **470**(2168), 20130847 (2014).

[29]C. Liu, Y. S. Gao, X. R. Dong, Y. Q. Wang, J. M. Liu, Y. N. Zhang, and N. Gui, "Third generation of vortex identification methods: Omega and Liutex/Rortex based systems," J. Hydrodyn. **31**(2), 205–223 (2019).

[30]T. Murata, K. Fukami, and K. Fukagata, "Nonlinear mode decomposition with convolutional neural networks for fluid dynamics," J. Fluid Mech. **882**, A13 (2020).